RHEO-PTV ANALYSIS OF COMPLEX FLUIDS

by

Ali Pourzahedi

BSc., Sharif University of Technology, 2016

A THESIS SUBMITTED IN PARTIAL FULFILLMENT OF

THE REQUIREMENTS FOR THE DEGREE OF

MASTER OF APPLIED SCIENCE

in

THE FACULTY OF GRADUATE AND POSTDOCTORAL STUDIES

(Mechanical Engineering)

THE UNIVERSITY OF BRITISH COLUMBIA

(Vancouver)

November 2018

The following individuals certify that they have read, and recommend to the Faculty of Graduate and Postdoctoral Studies for acceptance, a thesis/dissertation entitled:

Rheo-PTV Analysis of Complex Fluids

submitted by Ali Pourzahedi in partial fulfillment of the requirements for

the degree of Master of Applied Science

in Mechanical Engineering

Examining Committee:

Dr. Dana Grecov
Supervisor

Dr. Ian Frigaard
Supervisory Committee Member

Dr. Mu Chiao
Supervisory Committee Member

Abstract

Complex fluids are ubiquitous in the everyday life. Their study enables a better perception of the surrounding environment as it can be used to model a variety of industrial, biological and geophysical applications. This study presents a novel optical capillary rheometer that benefits from the advantages of both capillary rheometry and flow visualization.

The experimental setup developed in this research was applied to three different case studies, each highlighting an aspect of the rheological behavior of complex fluids. In the first case study, the slip mechanism of various concentrations of carbopol gel, as a simple yield stress fluid, was systematically investigated with respect to its material properties. Presence of a fully plugged flow and a thin layer of a Newtonian solvent, lubricating the unyielded gel at wall stresses below the yield stress was confirmed. The wall slip behavior of the carbopol gels at wall stresses above the yield stress was studied as well. It was shown that the slip velocities have a power-law correlation with the wall shear stress below the yielding point, and a linear correlation after the yielding point. Furthermore, the sliding threshold below which the gel sticks to the wall, was found to have a linear relationship with its yield stress and the fluidity of its solvent.

The start-up flow of laponite as a thixotropic yield stress fluid was examined in the second case study. The time dependent behavior of the fluid was studied in terms of the variations of shear stress at a constant flow rate. Finally, the behavior of synovial fluid at high shear rates was investigated as the third case study. Synovial fluid of the knee joint undergoes extensive range of shear rates during high physical activities. Rheological behavior of synovial fluid was studied at shear rates as high as 7000 s^{-1}, which is seven times greater than the maximum shear rate typically

measurable by a rotational rheometer. The method developed in this research enables to further study the complex behavior of fluids that are challenging using the conventional rheometry methods.

Lay Summary

Rheology is the science of deformation and flow of complex fluids such as polymers, foods, cosmetics and suspensions. Its expanse of application can range from industrial to biological to geophysical settings. Rotational rheometers have been the main apparatus for measuring the rheological behaviors of materials; however, there are certain cases where studying complex fluid flow behavior using the conventional rotational rheometry method will result in erroneous measurements or would not be feasible at all. The objective of this study is to provide a better understanding of these instances and pave the way to address the limitations of this method by developing a novel capillary rheometer integrated with a flow visualization unit. The developed method in this study has shown to have the potential to provide a greater insight into the complex behavior of fluid flow.

Preface

The research presented in this thesis was conducted by the author, Ali Pourzahedi, under supervision of Dr. Dana Grecov. The experimental setup design and material preparations were all done by the author except as specified below:

The CNC samples used in chapter 2 were provided by MohammadJavad Shariatzadeh. Masoud Daneshi helped with the post-processing of the flow visualization data presented in chapter 3, as well as the troubleshooting of the experimental setup. The synovial fluid samples used in chapter 4 were aspirated by Dr. Bassam Masri.

Results presented in chapter 3 will be submitted for publication; A. Pourzahedi, M. Daneshi, D. Grecov, M. Martinez, "Characterizing wall slip behavior of carbopol gels in a fully-developed Poiseuille flow".

Part of chapter 3 was presented as a poster in the 12th Annual European Rheology Conference (AERC) in Sorrento, Italy on April 17, 2018; A. Pourzahedi, M. Daneshi, D. Grecov, "Rheo-PTV analysis of yield stress fluids", page number 149 of conference abstract book.

The collection of synovial fluid from human subjects in chapter 4 were approved by the University of British Columbia Research Ethics Board (H08-02272). This ethics approval was originally drafted and submitted by Anwar Madkhali.

Table of Contents

List of Tables

List of Figures

List of Symbols

A	Cross-sectional area of the tube	[m^2]
R	Radius of the tube	[m]
R_p	Radius of soft particles	[m]
D	Diameter of the tube	[m]
L	Length of the tube	[m]
L_e	Entrance length	[m]
δ	Thickness of the slip layer	[m]
ρ	Density of the fluid	[$kg/m^{3]}$
μ	Dynamic viscosity of the fluid	[Pa.s]
μ_s	Dynamic viscosity of the solvent	[Pa.s]
Re	Reynolds number	[-]
ΔP	Pressure drop along the tube	[Pa]
Q	Flow rate	[m^3/s]
Q_s	Flow rate due to slip	[m^3/s]
$V_{avg,max}$	Maximum average velocity	[m/s]
U_s	Slip Velocity	[m/s]
U_m	Mean velocity	[m/s]
U^*	Slip velocity at the yielding point	[m/s]
K	Consistency factor	[$Pa.s^n$]

K_s	Solvent consistency factor	[Pa.s^n]
n	Power-law index	[-]
n_s	Solvent power-law index	[-]
G_p	Elastic modulus of soft particles	[Pa]
G_0	Bulk elastic modulus	[Pa]
τ_w	Wall shear stress	[Pa]
τ_y	Yield stress	[Pa]
τ_{sy}	Sliding yield stress	[Pa]
τ_{ij}	Deviatoric stress	[Pa]
$\|\|\tau\|\|$	Second invariants of the stress tensor	[Pa]
γ_y	Yield strain	[-]
$\dot{\gamma}_a$	Apparent shear rate	[s^{-1}]
$\dot{\gamma}_{true}$	True shear rate	[s^{-1}]
$\dot{\gamma}_{ij}$	Strain rate tensor	[s^{-1}]
$\|\|\dot{\gamma}\|\|$	Second invariants of the strain rate tensor	[s^{-1}]

Acknowledgements

I would like to thank my advisor, Dr. Dana Grecov, for her continued guidance, motivation and patience. I am very grateful to have had the opportunity to work with you. I would also like to thank Dr. Mark Martinez and Dr. Boris Stoeber for providing the access to the equipment required for my experimental setup.

I am very thankful to George Soong for his help with the lab equipment and providing a safe environment for everyone to work. I must thank all the members of the Industrial and Biological Multiphysics Laboratory (IBML) group and officemates for all the support they have given me. My sincerest thanks to Nick Yeh and Behzad Zakani for their patience in training me on the Kinexus rheometer and Somesh Bhatia for his helpful suggestions during the course of this study. I will be forever grateful to my friend Masoud Daneshi for his help throughout this project and for his patience with my endless questions.

Most importantly, my deepest gratitude to my parents, Hossein and Forouzan, and my sister Leila, for their endless love, support and encouragements in these past years. Words cannot describe how grateful I am for the opportunities you have set before me.

Dedication

To my beloved grandmother.

Chapter 1:

Introduction

Complex fluids are widely applied in daily life, as well as industrial and medical technologies, yet their intricacies are not fully understood. We are surrounded by these fluids on a daily basis. Tooth paste, shaving cream, ketchup, paint, cement, polymers and biological fluids are only a few examples, all of which show non-Newtonian behaviors. Industries dealing with food and beverages, cosmetics, medicine, oil and gas, polymer processing, lubrication and tribology, all require knowledge on the behavior of non-Newtonian fluids. In fact, one of the main goals in all these industries is to engineer materials with the desirable rheological behavior, adjusted to a specific application. It is noteworthy to mention few examples to better elucidate the role of rheology in different industrial and biological applications. One of the main applications of rheology appears in the oil and gas industry. Better understanding of the rheological behavior of the cement and mud used in the drilling operations leads to better well control and potentially prevents catastrophes such as the oil spill of 2010 in the Gulf of Mexico, which led to millions of gallons of oil spilling to the ocean, polluting the environment. In addition, most biological fluids are classified as non-Newtonian fluids. Many studies have been focusing on the role of rheology in the nature. For instance, rheological analysis has shown that the mucus layer secreted from underneath of a snail plays a key role in both its adhesion and locomotion [1]. Also, analyzing the rheology of spider silk allows creating novel synthetic materials with properties matching those of

natural spider silk [2]. Learning the expanse of applications within this field helps to better understand the surrounding nature, and imitating it, enables to find answers to complex problems that were solved by the nature thousands of year ago throughout evolution.

1.1 Motivations and Objectives

Rheometers are the main tool for measuring material characteristics. Several methods have been developed so far for finding the rheological behavior of materials. The most common methods could be categorized into drag flow rheometers and pressure-driven rheometers[1]. In drag flow rheometers, also known as rotational rheometers, the angular motion of a surface shears the sample. Parallel disk, cone and plate, Couette (cup and bub) are the common geometries used in drag flow rheometers. Pressure-driven rheometers generate shear by applying a constant pressure along a capillary tube, slit or axial-annulus [3], [4]. Each method has its own merits. Although rotational rheometers are ideal for analyzing the temperature and dynamic responses of the materials, capillary rheometers have the advantages of consuming less sample volumes, achieving high range of shear rates ($\sim 10^5\ s^{-1}$) and having less evaporation and contamination of samples over rotational rheometers. Moreover, they can easily be integrated with flow visualization techniques. The drawback of the capillary rheometers, however, is that the data processing is time consuming and requires multiple corrections (i.e. no real-time analysis). In addition, studying the time dependent responses of materials could be challenging. Non-compatibility with very viscous or stiff materials such as asphalt would also be another issue [3]–[5].

[1] Only shear rheometry is of concern in this study.

Aside from its advantages, the rotational rheometry method is not capable of capturing all the complex fluid behaviors. Examples of this would manifest in explaining the role of wall slip in the coating process and polymer extrusion, the role of thixotropy and wall slip in the transport of waxy crude oil in a pipeline, and the role of shear dependent rheology of synovial fluid in the joint lubrication. Furthermore, the results obtained from the rotational rheometry method are prone to artifacts caused by effects such as wall slip and shear banding [6], [7]. The main objective of this study is to address the limitations of the conventional rheometry in complex fluid analysis by proposing a novel capillary device that benefits from the advantages of both capillary rheometry and flow visualization techniques. Therefore, any effect due to the flow configuration (e.g. wall slip and shear banding) on the rheological behavior of the materials could be detected and visualized. There have previously been studies in the literature that integrated the rotational rheometry [8], [9] or the capillary rheometry [10]–[12] as the viscometry unit, with a flow visualization unit, where the knowledge of the flow kinematics was required in addition to the rheological properties of the materials. In this research, the capability of the proposed method in measuring and visualizing the complex fluid behaviors is assessed by analyzing the internal flow of simple yield stress and thixotropic yield stress fluids, as well as biofluids, as case studies that would be challenging to analyze using the conventional rotational rheometry methods. The specific objectives and description of the case studies are presented in the following:

1. **Investigating the slip mechanism of carbopol gel.**

   Dynamics of the flow are not only dependent on the fluid rheology and geometry of conduit, but also dependent on the fluid-solid interactions. One of the major characteristics of the complex fluids is having slip velocity at the wall surface [13]. This behavior

especially helps while pumping complex fluids in a pipeline. However, having slip might lead to erroneous results while measuring the rheological properties of the fluids [14], [15]. In practice, in many geophysical and industrial settings, this fluid-solid interaction in terms of slip velocity might lead to localization and channelization of the flow [16]. In this case study, the focus is on the slip behavior of carbopol as a microgel paste. Many efforts have been done so far in the literature to better understand the slip behavior of this type of material; however, a systematic analysis of the slip regimes with respect to the material properties is still lacking. This case study aimed to investigate the effect of wall slip on the flow configuration of carbopol gels as a simple yield stress fluid, to develop a model for wall slip as a function of the wall shear stress and the material properties. Furthermore, the behavior of the sliding yield stress, the stress at which the fluid starts to flow, with respect to material properties was systematically studied.

2. **Analyzing the start-up flow of laponite.**

   Another characteristic of complex fluids is having a time dependent rheological behaviors. In order to evaluate the ability of the proposed method in capturing the time dependent behavior of complex fluids, start-up flow of laponite, as a thixotropic yield stress fluid was investigated in this case study. The start-up flow is a major concern especially in oil and gas industry, were restarting the flow in the pipeline after shutdown of the well becomes a significant issue [17], [18].

3. **Investigating the rheological behavior of synovial fluid at high shear rates.**

   One of the major limitations of the rotational rheometers manifest while dealing with biofluids. Biofluids usually have lower values of viscosities, therefore, to generate

sufficient torque, larger geometries have to be used which leads to larger sample volumes required. The experimental challenges with biofluids typically arise from the low sample volumes and the possibility of contamination and evaporation of the samples, which could have an effect on its rheological properties. Moreover, finding a suitable biofluid donor is typically not an easy task, therefore, it is of utmost importance to obtain the most data out of each sample provided [5], [19]. In this study, synovial fluid was chosen as a case study for biofluids due to its interesting non-Newtonian behaviors. Synovial fluid is the lubricant and shock absorber in the joints. It has been found that the diseased synovial fluids exhibit different rheological characteristics in comparison to the healthy ones (e.g. lower viscosity). Hence, rheological study of synovial fluid could lead to a better understanding of diseases associated with synovial fluids, known as arthritis. In this case study, synovial fluid of the knee joint is of interest. A key feature in the rheological analysis of synovial fluid is that it should be tested at high range of shear rates to resemble the actual conditions inside the joint, as the shear rate could increase up to 10^5 s^{-1} in the knee joint while running [20], [21]. Capillary rheometers are able to reach high shear rates without creating turbulence, inertial instabilities, secondary flows or interfacial artifacts, typically associated with the rotational rheometry measurements.

1.2 Outline of the Thesis

Chapter 2 of this thesis describes the details of the experimental setup, which consists of both viscometry and visualization units. The techniques used for analyzing the data gathered from each unit are explained in detail. The method used to benchmark each unit is also presented.

Chapter 3 and chapter 4 present three case studies where the proposed capillary rheometer is used to address the limitations of the conventional rotational rheometry. Chapter 3 is designated to the study of the complex phenomena in internal flow of yield stress fluids, i.e. wall slip and time dependent behaviors. Chapter 4 is dedicated to the study of biofluids.

Chapter 5 provides a summary of the main contributions of this study, discusses the limitations and presents suggestions for the potential future work.

Chapter 2:

Experimental Design

2.1 Introduction

In this chapter, the experimental setup of the proposed capillary rheometer and the science behind it is described in detail. The experimental setup comprises a viscometry unit as well as a flow visualization unit. The method used for analyzing the data obtained from each unit is explained at the end of this chapter. After the design of the experimental setup, its capability to accurately measure the rheological properties of the materials is verified by benchmarking it with both Newtonian and shear thinning fluids of known properties. Results of the viscometry unit are found to be in good agreement with the data obtained from the rotational rheometry. In addition, the results obtained from the flow visualization unit follow the expected analytical behavior as well as the no-slip boundary condition at the wall location.

2.2 Experimental Setup

2.2.1 Viscometry Unit

The viscometry unit of the experimental setup is designed to measure the flow curve of fluids, which is essentially finding the relationship between the shear stresses and the shear rates of the

material. This unit consists of a syringe pump (kdScientific) with 0.5% full scale accuracy and pressure sensor (Elveflow) with 0.2% full scale accuracy. Two sets of pressure sensors, one with a range of 340 mbar and another with a range of 2 bar were used to have sufficient accuracy for various fluid viscosities. The pressure sensors were connected to a data acquisition system (Elveflow) with acquisition resolution of 11 bit and acquisition frequency of 10 kHz. The data acquisition system is then connected to a computer for data post-processing.

Two sets of capillary tubes were used in the experiments to address various viscosity and shear rate ranges. An optically smooth triangular borosilicate glass capillary tube, as shown in Figure 2.4, with a diameter of 1.16 mm and a length of 381 mm was used as the flow conduit for case studies 1 and 2 (chapter 3). A stainless-steel tube with a diameter of 0.254 mm and a length of 914.4 mm was used in case study 3 (chapter 4), for studying low viscosity biofluids at high shear rates. A schematic view of the viscometry unit is depicted in Figure 2.1. It is worth mentioning that glass syringes as well as hard plastic tubes for connections from the syringe pump all the way to the capillary tube were chosen, to avoid added response time to the system due to the elasticity of the equipment.

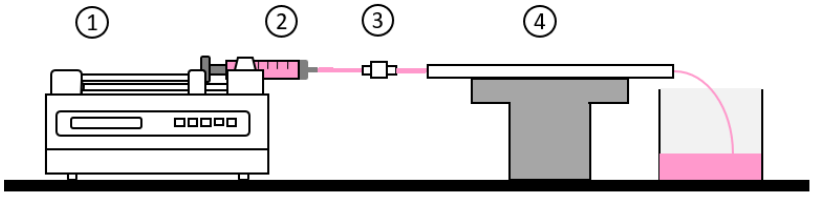

Figure 2.1) Schematic of the viscometry unit: 1) Syringe pump, 2) syringe, 3) pressure sensor, 4) capillary tube.

The diameter of the borosilicate capillary tube was measured precisely using a confocal microscope with a resolution of 0.65 µm due to the wide range of tolerances given by the

manufacturer. The resolution of the stainless-steel diameter was reported as 10 μm by the manufacturer, which is acceptable for the purpose of this study. Figure 2.2 demonstrates the cross-sectional image captured using the confocal microscope.

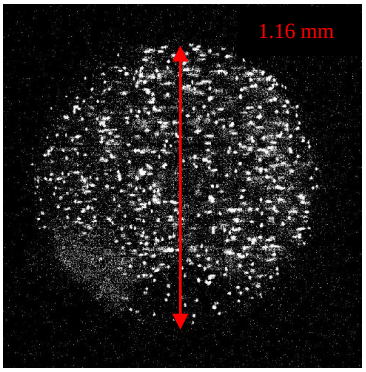

Figure 2.2) Cross-sectional image of the borosilicate glass capillary tube obtained from the confocal microscope.

Pressures of yield stress fluids cannot be measured with the common differential pressure sensors, since a stagnation region will create near its sensing diaphragm and the fluid will jam and turn into solid, thus, unable to convey pressure to the sensor. Therefore, in-line pressure sensors are the suitable choice for the type of fluids used in this study (see Figure 2.1).

Slender conduits provide high shear rate ranges, which is of interest in case study 3 of this study (chapter 4). Circular capillary tubes and Hele-Shaw cells are among the geometries that are able to produce high shear rates, have unidirectional flow and calculation of rheological properties are relatively simple in them. Between the two aforementioned geometries, circular capillary tubes were chosen for the viscometric measurements as opposed to rectangular Hele-Shaw cells due to the following reasons:

- It has been shown that flow of viscoplastic fluids are susceptible to be channelized and to have non-uniform flow configurations along narrow slots [16]. This does not occur in circular capillaries due to their axisymmetric geometry.
- Fluid-solid interaction is important in this study since wall slip is of concern. It is easier to control surface properties in circular capillaries. In Hele-Shaw cell, a large surface is exposed to the fluid flow and slight non-uniformities on the surface would lead to change in flow configuration.
- Circular capillaries are less prone to deformation as opposed to channels at high pressures.
- Circular capillaries can be easily integrated with the in-line pressure sensors without any significant pressure loss, whereas in order to connect a channel to the pressure sensors, a 90° bend at the inlet of the channel is required which would create a considerable pressure loss.
- Finally, it is much easier to clean a capillary tube in comparison to a channel.

2.2.1.1 Sealing

One of the major challenges of every fluid mechanics related experimental setup is to seal it from any possible leaks throughout the system. Leaks can lead to under-estimation of pressure measurements as well as loss of sample volume. In the experimental setup designed in this study, the challenge of connecting the triangular capillary and the circular plastic connection tube was overcome by creating a plastic connector out of Acrylonitrile Butadiene Styrene (ABS) using the Afinia H480 3D-Printer. The connector was designed to cover the triangular surface of the capillary tube at one end and fit in the plastic tube at the other end. It should be noted that the

connection does not go through the inner circular surface of the capillary tube, since it would cause the fluid to undergo excess pre-shear before entering the capillary tube and impact its rheology. The connection points at both ends were glued afterwards to add further sealing to the capillary inlet. The connector image and schematic are depicted in Figure 2.3. The designed sealing system was able to withstand pressures in the order of 3 bar throughout the experiments.

It should be mentioned that sealing of the stainless-steel tube was not as challenging and simply gluing the plastic tubing with the capillary tube was sufficient.

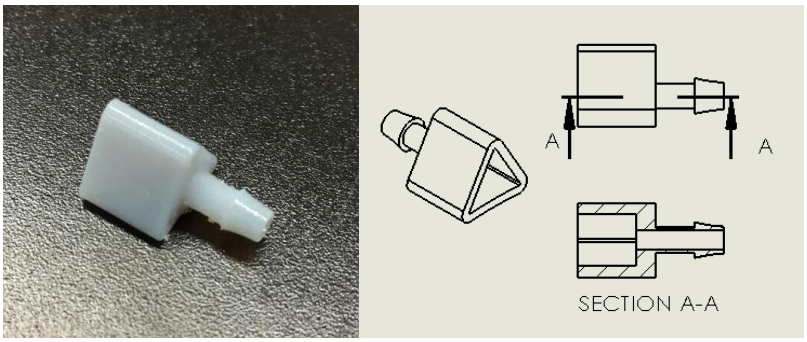

Figure 2.3) Actual and schematic view of the sealing connector between the triangular borosilicate capillary and the plastic tube.

2.2.2 Flow Visualization Unit

Optical Coherence Tomography (OCT) from Thorlabs (TEL1300V2-BU) was used to visualize and capture the image sequences of the seeded flow provided by the syringe pump. OCT is an optical, non-invasive and contactless imaging tool which is capable of visualization in opaque fluids as well. In OCT, the low coherence length light source is split into and recombined from the reference and sample mirrors to form the interference pattern back-scattered from the specimen.

This interference pattern provides details such as the location and velocity of the scattering particles [22]–[26].

The flow visualization unit is demonstrated in Figure 2.4. OCT generates vertical collimated beam with a Gaussian shape (center wavelength of 1300 nm). It provides cross-sectional images along the z axis (x–z or y–z plane). The depth of view in the z direction (A-scan) is 3.6 (mm) with a resolution of 4.2 (µm). The lateral resolution (B-scan) is the same as the thickness of the light beam which is 13 (µm) [27]. In addition, OCT has a high temporal sensitivity (up to 76 kHz). In this study, the time frame intervals were adjusted between 20 – 223 ms depending on the flow rates. A hybrid PIV+PTV method [28], [29], described in details in section 2.3.2, was applied using LaVision–DaVis software for post-processing the image sequences captured by the OCT in order to find the velocity field.

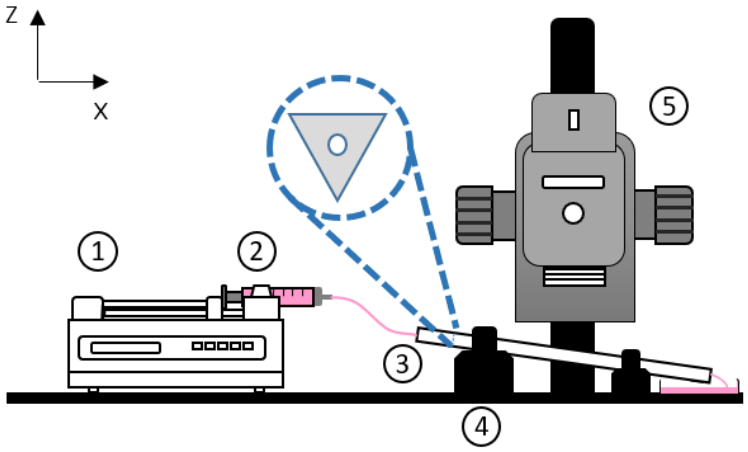

Figure 2.4) Schematic of the flow visualization unit: 1) Syringe pump, 2) syringe, 3) capillary tube, 4) base for creating a 5° angle with horizontal direction, 5) OCT. The capillary tube has a triangular cross-section as shown.

All fluids in this study were seeded with polystyrene microspheres (Magsphere Inc.) with a diameter of 4.05 ± 0.16 μm and density of 1.05 g/cm^3 according to the following protocol:

- The particle container was well-shaken for 3 minutes at 1000 rpm using a vortexer (Fisher Scientific) to make a homogenous suspension and sonicated afterwards for 5 minutes to detach the agglomerated particles.
- 1 μL of particle was added for every 1 mL of fluid sample (this ratio was found after multiple trial and errors of flow visualization).
- The seeded fluid was intensely shaken by hand for two minutes to initially disperse the particles and then the vortexer was used for 5 minutes to release any residual stresses in the fluid sample.
- The seeded fluid was sonicated for 6 minutes and degassed for 3 minutes at the end.

Sonication and degassing were performed using Branson 2800 ultrasonic bath to disrupt aggregates and achieve uniform dispersion. Volumetric concentration of the particles inside the samples were less than 0.1%; therefore, their impact on the sample rheology is negligible.

A triangular borosilicate glass capillary tube, as shown in Figure 2.4 and described earlier, was chosen as the flow conduit so that the light beams could penetrate through the tube and get recaptured after reflecting from the seeding particles without getting refracted. It should be noted that the refractive index of the borosilicate glass capillary tube and the fluids used in the experiments are approximately the same (~ 1.4); therefore, the refractions between the fluid and the inner wall surface boundary of the capillary tube are negligible. The capillary tube is also slightly tilted at an angle of 5° using two stands created with the 3D-printer. This is to maximize the reflections from the tracing particles and minimize the reflections from the side wall. A sample

image of tracing particles taken by the OCT is shown in Figure 2.5a. Figure 2.5b illustrates the flow streaklines which are obtained by superimposing 1000 frames of OCT images. All the measurements and velocity profiles were obtained from the x–z plane that passes through the centerline of the tube. The OCT lens was focused on the centerline of the capillary tube by moving the x–z plane along the y axis to find the limits of the inner wall in the y direction. Now by knowing the position of the walls, the centerline would be the average distance between the two (see Figure 2.4).

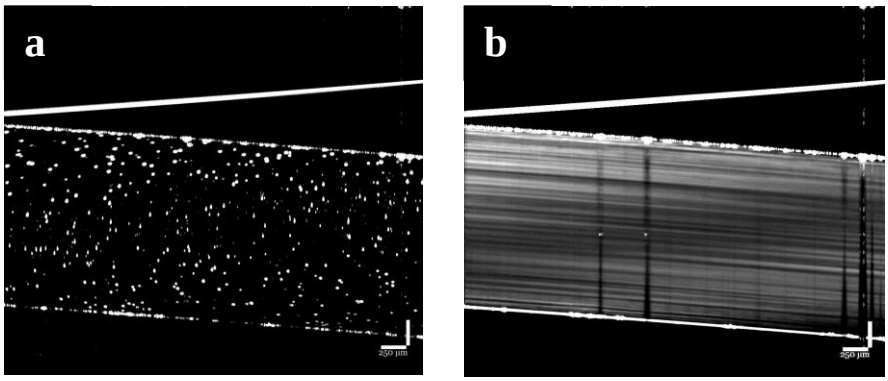

Figure 2.5) (a) A sample OCT image, (b) Flow streaklines obtained by superimposing 1000 OCT frames. The scaling dimension of the images is 250 μm. The additional line observed above the tube is the reflection of the bottom wall inside the top wall.

Since the fluid inside the experimental setup flows from a larger conduit (syringe and the connection tubes) to a smaller one (capillary tube), it is important to consider the entrance length effect to make sure whether the visualizations were done in the fully-developed regime of the flow. The OCT lens was focused on the middle of the length of the capillary tube. For low Reynolds numbers ($Re < 2000$) the entrance length could be estimated as [30], [31]:

$$L_e = D\left(\frac{0.6}{1+0.035\,Re}\right) + 0.056\,Re \tag{2.1}$$

where D is the tube diameter. In order to find the upper limit of the Reynolds number in the experiments, calculations are presented for water as the working fluid. The maximum range of flow rate used throughout the experiments (in both viscometry and flow visualization) was Q = 4 mL/min. Therefore, the maximum average velocity in the capillary tube could be calculated as:

$$V_{avg,max} = \frac{Q}{A} = \frac{4\ (mL/\text{min})}{\pi \times \frac{1.16^2}{4}\ (mm^2)} = 63.1\ mm/s$$

where Q is the flow rate and A is the cross-sectional area of the tube. Now, the Reynolds number can be calculated as follows:

$$Re = \frac{\rho V_{avg} D}{\mu} = \frac{1000\ (kg/m^3) \times 63.1\ (mm/s) \times 1.16\ (mm)}{0.001\ (Pa.s)} = 73$$

where ρ and μ are the fluid density and dynamic viscosity respectively. *Re* number is found to be much smaller than the critical value of 2000. As a result, the entrance length would be L_e = 4.3 mm. That is around 1% of the entire length of tube (381 mm). Thus, the flow visualization is certainly being done in the fully developed region of the flow.

It should be emphasized that by using the same procedure for the stainless-steel tube, the maximum average velocity ($V_{avg,max}$) obtained is 1316.4 mm/s and the subsequent Reynolds number would be 334. Thus, the entrance length (L_e) would result in 18.8 mm, which is 2% of the entire tube length (914.4 mm). Therefore, in general, the entrance length effect could be neglected in this

study. Moreover, due to the large *L/D* ratio, end entrance pressure correction (also known as Bagley correction) on the wall shear stress are not considerable and can be neglected.

It should be mentioned that after each viscometry or flow visualization experiment, the capillary tube and the pressure sensor were cleaned by circulating water and isopropyl alcohol followed by drying with compressed air.

Various instruments have been used in the literature so far for flow visualization purposes, including PIV, Micro-PIV, LDV and UDV. In this study, conventional PIV along with laser and CCD camera was not used, since the diameter of the capillary tube is too small, and details of the velocity profiles cannot be captured. Micro-PIV was not used as well, since the recording frequency is low in this method and the particles will travel out of the measurement window quickly. In addition, in Micro-PIV, a volume of fluid is illuminated and the plane of measurement has a considerable thickness, leading to high errors and underestimation of the velocities. Furthermore, the capillary tube would not fit in the Micro-PIV stage. LDV (Laser Doppler Velocimetry) or UDV (Ultrasonic Doppler Velocimetry) were not suitable methods for the purposes of this study, due to their low resolution near the wall (200 μm) [32], [33]. On the contrary, OCT has low working distance, small measurement plane thickness and high spatial and temporal resolution. Moreover, it is easy to integrate it with the rest of the experimental setup used in this study. Thus, using OCT as the flow visualization tool for this study would be a proper choice.

2.3 Data Analysis

2.3.1 Viscometry Analysis

Capillary viscometers work based on measuring pressure drops across a straight tube for known imposed flow rates (or vice versa). The expression derived for the viscosity is based on the properties of the fluid near the wall and could be written as follows [4], [5], [11], [31]:

$$\tau_w = \frac{\Delta P.R}{2L} \tag{2.2}$$

$$\dot{\gamma}_a = \frac{4Q}{\pi R^3} \tag{2.3}$$

$$\dot{\gamma}_{true} = \frac{\dot{\gamma}_a}{4}\left[3 + \frac{d\ ln(\dot{\gamma}_a)}{d\ \ln(\tau_w)}\right] \tag{22.4}$$

where τ_w, $\dot{\gamma}_a$, $\dot{\gamma}_{true}$, ΔP, Q, R and L are the wall shear stress, apparent shear rate at the wall, true shear rate at the wall, pressure drop along the tube, flow rate, radius and length of the tube respectively. Dynamic viscosity (μ) could be easily found by dividing the shear stress by the true shear rate. The derivative in Equation 2.4 is the slope of apparent shear rate to the wall shear stress on a log-log scale, known as the Weissenberg-Rabinowitsch-Mooney (WRM) correction factor [4], [31]. It should be noted that for a Newtonian fluid, this derivative is unity and the apparent shear rate and the true shear rate would be equal [5]. In case of presence of slip at the wall, the flow rate, "Q", has to be replaced with the net flowrate, "$Q - Q_s$", where "Q_s" is the flow rate due to slip [11]. The corrected shear rate formulation is valid for any type of generalized Newtonian fluid. Details on how to derive Equations 2.2 – 2.4 are described in Appendix A.

2.3.2 Flow Visualization Analysis

Velocity profiles provide important information on the complex fluid flow behavior (e.g. wall slip, shear banding, time dependent behavior, etc.). Several techniques have been used in the literature for finding the velocity field of fluids inside the channels and capillaries, among which particle-based visualization has gained much attention recently [34]. This method involves finding the velocity profiles by following the marker particles in a seeded fluid. The two widely used particle-based techniques are particle image velocimetry (PIV) [11], [35], [36] and particle tracking velocimetry (PTV) [25], [36].

In PIV, which is based on the Eulerian approach, the images of an ensemble of particles from two consecutive time steps of an interrogation window are statistically compared to each other using a spatial cross-correlation function to find the average shift in the particle locations. Knowing the time delay between the two consecutive frames, the average velocity of the interrogation window could be found [32], [33], [34].

PTV uses the Lagrangian approach of tracing the motion of individual particles. In this method, the particles are detected by first subtracting the background noise from the images and then searching for local maximum intensities at each frame. The particle positions are paired between two consecutive frames based on the minimum distance criterion. The velocity of each particle again could be easily found by knowing the time interval between the two consecutive frames [32], [33], [34].

In comparison to PTV, PIV has the advantage of being more robust and less prone to errors and invalid measurements due to the mismatch in pairing the images of the particles, since it averages

the motion of a group of particles. PTV gives a velocity vector for each particle, thus, larger number of frames are required in order to eliminate the spurious velocity vectors. Since PIV takes averages of each interrogation window, it will not be ideal for measuring the near wall velocities, whereas PTV has the advantage of higher resolution that is down to the size of the particles [28], [32]–[34].

In this study, although computationally more time consuming, a more accurate method was performed using the LaVision-DaVis software, by integrating the interrogation analysis of a group of particles using PIV as a guidance for PTV analysis, known as "super-resolution particle image velocimetry" method to benefit from advantages of both approaches to find the velocity field. In this technique, the velocity gradient results obtained from PIV provide an estimate of the displacement field and search areas which are then used in the PTV analysis to reduce the number of cross-correlation iterations [28], [29], [34].

2.4 Benchmarking

2.4.1 Material and Rheology

In order to examine the accuracy of the experimental setup, water-glycerol solution as a Newtonian fluid and cellulose nanocrystalline (CNC) suspension as a shear thinning fluid were prepared as follows. Water-glycerol solution with a concentration of 31% (wt/wt) was used so that its density matches the density of the tracing particles (i.e. 1.05 g/cm^3). For preparing CNC aqueous suspension, CNC powder (CelluForce) was mixed with distilled water to make a 2% (wt/wt)

concentration. The sample was sonicated at 1000 J/g using an ultrasonic processor VCX-130 (Sonics & Materials) to homogenize the suspension [37], [38].

Rheological properties of the materials were measured using Malvern Kinexus rotational rheometer with angular resolution of 10 nrad and torque resolution of 0.05 nN.m. Parallel plate geometry with a diameter of 60 mm and a gap distance of 1 mm was used for this purpose. All tests were conducted at room temperature (25 °C).

Viscometry tests were conducted by first pre-shearing the samples at shear rate of 50 s^{-1} for 30 s and then measuring the steady-state stress at each given shear rate. Flow curves of the water-glycerol and the CNC suspension obtained from the rotational rheometer are shown in Figure 2.6 with red marks.

2.4.2 Viscometry Unit

Viscosities were calculated using the borosilicate capillary tube and with the formulation shown in Equations 2.2 – 2.4. Results comply well with the results obtained from Malvern Kinexus rotational rheometer as shown in Figure 2.6. As demonstrated, water-glycerol solution showed a constant viscosity throughout all range of shear rates. Rheological behavior of CNC can be modeled as a power-law fluid. It is worth mentioning that much higher shear rates were achieved by the capillary rheometer (~ 7000 s^{-1}) in comparison to the rotational rheometer. The larger error bars at low shear rates (flow rates) are due to the higher errors in the pressure measurements close to the sensor lower bound limit.

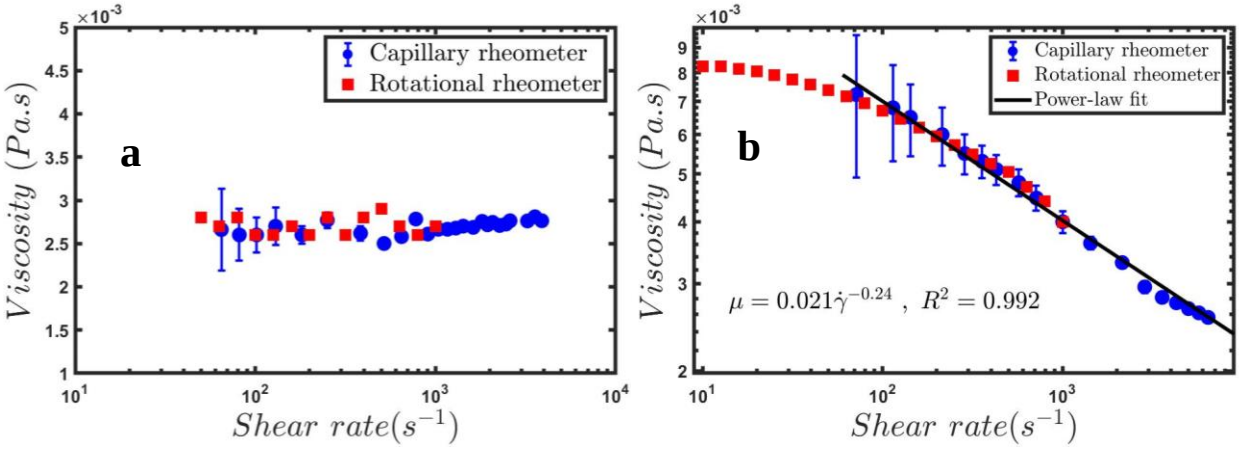

Figure 2.6) Viscosity benchmarking. (a) Water-glycerol 31% shows constant viscosity at all shear rates, (b) CNC 2% follows a power-law viscosity model. Red marks indicate data from the rotational rheometer and blue marks indicate results from the capillary rheometer. The solid black line represents the best power-law fit to the data obtained from the capillary rheometer which can be formulated as $\mu = 0.021\dot{\gamma}^{-0.24}$.

2.4.3 Flow Visualization Unit

In post-processing the OCT results, wall positions were detected with a resolution of 10-15 µm by applying an edge detection algorithm to the average of image sequences using the Matlab software. As shown in Figure 2.5b, wall locations have higher intensity since they are fixed throughout all the images. Slip velocities were measured in post-processing the PTV results by linearly extrapolating the velocity data corresponding to the region within 50 µm of the wall, to the wall position [11], [35].

Figure 2.7a demonstrates the normalized velocity profiles of 31% water-glycerol solution for several flow rates. The results comply thoroughly with the analytical parabolic solution. The no-slip condition could also be observed at the wall location (see Figure 2.7b). Figure 2.8a illustrates

the velocity profiles of 2% CNC suspension. The velocity profiles also confirm the no-slip condition at the wall, in accordance with the results previously stated in the literature [39], [40]. In addition, flattened velocity profiles attributed to the shear thinning behavior of the fluid were captured. Flow rates calculated by integrating the area beneath the velocity profiles had a maximum deviation of 6% from the imposed flow rate by the syringe pump. This indicates that the proposed experimental method is fully capable of obtaining the velocity profiles and the slip velocities over a wide range of wall shear rates and regardless of the shear thinning effect. It should be noted that in all velocity profiles, the left wall corresponds to the top side of the tube and the right wall corresponds to the bottom side of the tube in Figure 2.4. Given the fact that less light is able to penetrate through and reflect back from the particles close to the bottom side of the tube, less data would be available there; thus, all the measurements were done based on the data available on the top side (left wall in the velocity profiles).

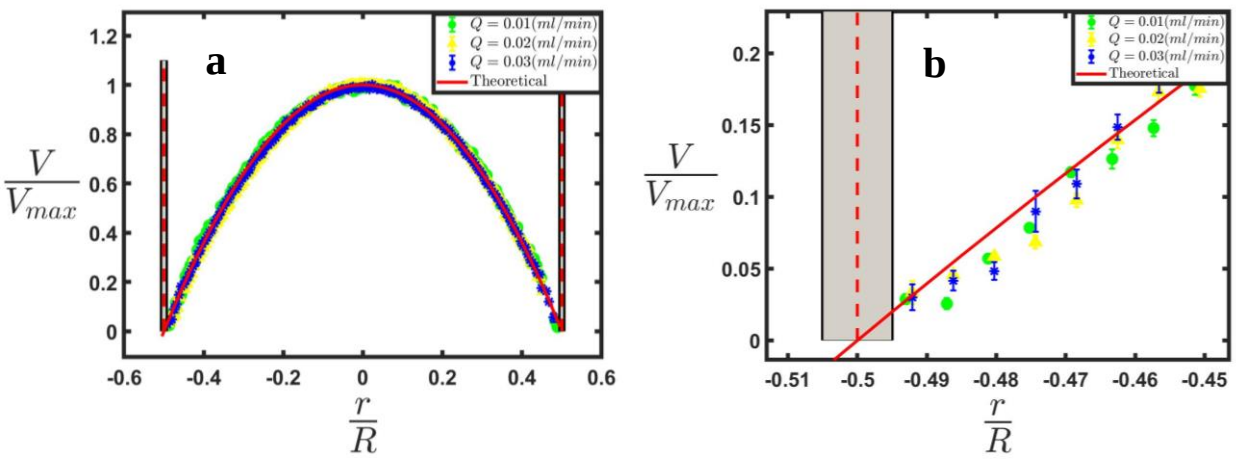

Figure 2.7) (a) Velocity profile benchmarking using water-glycerol 31% solution. The normalized velocities from all flow rates superimpose on each other. The solid red line shows the analytical parabolic velocity profile. (b) Velocity profiles of 31% water-glycerol solution 50 µm near the wall position.

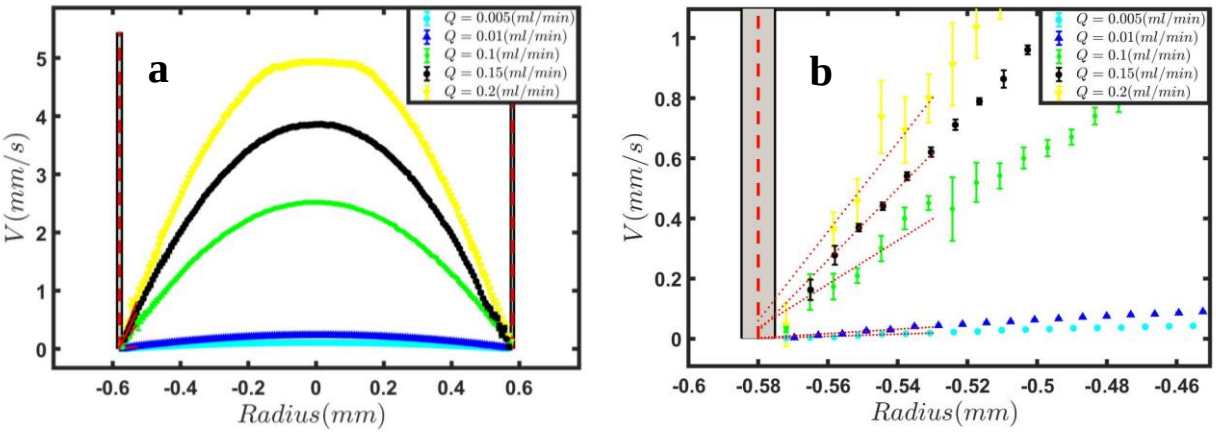

Figure 2.8) (a) Velocity profile benchmarking using CNC 2% suspension. (b) Velocity profiles of CNC 2% suspension near the wall. The dotted red lines represent linear extrapolation of velocity data in the 50 µm vicinity near the wall position.

As the Rheo-PTV experimental setup is completely designed and its accuracy is verified over a wide range of shear rates, it can be applied to study different test cases. Chapters 3 and 4 explore the capabilities of the developed Rheo-PTV device in the analysis of complex fluid behaviors by demonstrating its range of applications.

Chapter 3:

Internal Flow of Yield Stress Fluids

3.1 Introduction

Complex fluids are commonly known for their intricate characteristics such as wall slip, shear banding, time dependency, etc. [6], [7] which leads to inconsistency or time dependency between the stress and the shear rate in a simple shear fluid flow [41]. In this chapter, the proposed capillary rheometry method was used to better understand the wall slip behavior of carbopol as a simple yield stress fluid, and the time dependent behavior of laponite as a thixotropic yield stress fluid as case studies that would be challenging to analyze using a conventional rotational rheometry method.

3.2 Wall Slip Behavior of Carbopol Gel

3.2.1 Background

Concentrated dispersions including microgel pastes, granular suspensions and emulsions which exhibit viscoplastic behavior can be found in a wide variety of geophysical and industrial settings ranging from plumbing of mud volcanos to the recovery of oil [1]. The origin of solid-fluid like behavior of these materials roots in their closed packed amorphous structure which allows them to deform only if a shear stress larger than the yield stress is applied [42], [43]. However, the motion of these materials is not only a function of their bulk flow properties, but also is dependent on their interactions with the confining solid boundaries [1], [44]. In practice, viscoplastic fluids like many other complex fluids exhibit wall slip behavior, which is significant at their creeping flows and complicates their internal flow along thin conduits [11], [12], [16], [35]. There have been efforts in the literature to study the slip mechanism of yield stress fluids; however, there lacks a systematic approach to understand the effect of wall slip on the flow configuration in these fluids. This section characterizes the slip behavior of carbopol gels which are categorized under dispersion of soft particles. Carbopol solutions have been used in many rheological and hydrodynamic studies as a widely accepted model yield stress fluid due to their optical transparency, stability in time, and insignificant thixotropic and aging behavior [45]–[48].

The wall slip behavior in the flow of suspensions of rigid and soft particles is often attributed to migration of disperse phase away from the shearing surfaces. It leads to the formation of a dilute layer between the surfaces and the main body of the suspension which is known as apparent slip layer. The lubrication role of this depleted layer is interpreted as the slip behavior at macroscale

[13], [49]–[51]. As proposed by Kalyon et al. [50], with the presence of a stable and thin slip layer which solely contains a shear thinning solvent, the apparent slip velocity, U_s, can be related to the wall shear stress, τ_w, as follows,

$$\tau_w = \mu_s \frac{U_s}{\delta} \tag{3.1}$$

$$U_s = \delta \left(\frac{\tau_w}{K_s}\right)^{1/n_s} \tag{3.2}$$

where K_s is the solvent consistency, n_s is the solvent power-law index, and δ is the thickness of the slip layer. Therefore, the thickness of the slip layer is a key parameter in determining the wall slip as a function of rheological properties of the binder fluid and the wall shear stress.

Meeker et al. [8] presented a theory to explain the slip dynamics of suspension of soft particles based on hydrodynamic lubrication of elastically deformed particles on the shearing surfaces. They have assumed that the thickness of the slip layer is determined by the balance between the osmotic pressure of the suspension and the lubrication force caused by relative motion of shearing surfaces and particles, with the assumption of a Newtonian binder fluid, as follows,

$$\delta \sim \left(\frac{\mu_s U_s R_p}{G_p}\right)^{1/2} \tag{3.3}$$

where μ_s is the viscosity of the solvent, while R_p and G_p represent the radius of soft particles and their elastic modulus, respectively. Accordingly, Meeker et al. and Seth et al. [8], [9] proposed an experimental correlation for the scaled slip velocity below the yield stress, which is in accordance with the elasto-hydrodynamic lubrication theory,

$$\frac{U_s}{U^*} \sim \left(\frac{\tau_w - \tau_{sy}}{\tau_y - \tau_{sy}}\right)^2, \quad U^* \sim \frac{G_0 R_p}{\mu_s} \tag{3.4}$$

where τ_{sy} is the sliding yield stress, U^* is the slip velocity at the yielding point and G_0 is the bulk elastic modulus according to $\tau_y = G_0\gamma_y$, where γ_y is the yield strain. Applying a high resolution PTV technique, Seth et al. measured the slip velocity in the yielding regime and indicated that it will be correlated with the applied velocity, U_m, as $U_s \sim {U_m}^{0.27}$. In addition, they confirmed the insensitivity of the lubrication layer thickness to the wall stress beyond the yielding point [9]. Recently, by utilizing flow visualization devices integrated with a capillary viscometer, the wall slip behavior of microgel pastes have been examined in pressure driven flows. Gonzalez et al. and Aktas et al. [11], [35] studied the capillary flow of 0.2% carbopol solution and delineated that slip velocity increases with the wall stress through a power-law model in both unyielded and yielding regions, i.e. $U_s \sim {\tau_w}^{0.876}$. Moreover, Aktas et al. [11] indicated that the thickness of the slip layer measured by the steady torsional flow or estimated by the elasto-hydrodynamic theory underestimates the one measured in a capillary flow. They showed that in a capillary flow the slip layer thickness decreases by the wall shear stress, above the yielding point and interpreted it as the pressure or normal stress dependency of the slip layer thickness in the capillary flow. Overall, it can be concluded that the dynamics of the wall slip behavior of carbopol in capillary flow has not been understood well. Moreover, an inspection of the available literature on the slip behavior of carbopol in capillary flow does not confirm the universality of the correlation of wall slip reported by Gonzalez and Aktas [11], [12], [35]. Poumaere et al. [12] reported a nearly linear scaling of the slip velocity with shear stress, $U_s \sim {\tau_w}^{1.32\pm0.26}$, for flow of 0.08% carbopol along a glass capillary. However, Geraud et al. [52] reported a quadratic model for the variation of slip velocity with respect to the wall stress, i.e. $U_s \sim {\tau_w}^2$, for flow of 0.1% carbopol in a Hele-Shaw cell made of glass. The discrepancies between the models reported in the literature was a motivation to revisit the problem and assess the generality of wall slip behavior in the case of capillary flow of carbopol

microgels. Regarding the available literature on the wall slip of carbopol, one could assume that the wall slip is a function of shear stress at the walls as well as the rheological properties of the fluids, for the same shearing surfaces. This section is aimed to provide a general form of correlation for the wall slip and sliding yield stress of the carbopol gels in a capillary flow.

3.2.2 Materials and Rheology

Various concentrations of aqueous solutions of carbopol 940 were used as a microgel paste in this study. Each sample of carbopol solution was prepared as follows. First, carbopol powder was dispersed in five litters of distilled water. The mixture was stirred gently with a propeller mixer at 120 rpm until the carbopol powder was dissolved homogenously. Adding carbopol to the water causes the release of H^+ ions and decrease in the pH of the solution. Then, 5% aqueous sodium hydroxide (NaOH) was gently added to the solution in order to bring its pH to a neutral value. Then, the mixture was stirred by a propeller mixer for 48 hours at a low mixing rate of 300 rpm. The solution was kept at rest for 12 hours and its final pH value was monitored by a pH meter [11], [12], [35], [52], [53]. In addition, carbopol gel 0.1% with glycerol solution as the solvent was prepared to investigate the effect of solvent viscosity on the slip of microgels. Same procedure described above was followed with the exception that carbopol powder was mixed in 31% glycerol solution instead of water. Furthermore, a new carbopol solution was prepared by stirring a 0.1% carbopol gel with a sharp blade at 1200 rpm, for three minutes which would lead to the breakdown of its structure. This highly sheared solution was prepared to study the effect of mixing rate and fluid structure on the slip of microgels.

Rheological properties of the carbopols were measured using Malvern Kinexus rotational rheometer. A parallel plate geometry with a diameter of 60 mm and a gap distance of 1 mm was used for measuring the rheological characteristics of the materials. Sand paper with a roughness of 46 µm was attached to both plates to minimize the effect of wall slip. All tests were conducted at the room temperature (25 °C). A series of shear rate-controlled tests for the shear rates in the range of 10^{-4} to 100 s^{-1} were performed to determine the flow curve of the samples. Before starting the tests, the samples were pre-sheared at 100 s^{-1} for 60 s followed by 120 s of resting period. The rheological experiments started with an increasing shear rate ramp and ended with a decreasing shear rate ramp. The increasing-decreasing ramps were repeated without delay for two times. The shear stress corresponding to each point of the flow curve has been averaged over 5 s (larger averaging time periods was found to not change the flow curves). The flow curves associated with the decreasing shear rate ramps are shown in Figure 3.1. It should be mentioned that the data regarding the repeated ramp tests superimposed. In addition, the flow curves corresponding to the increasing and the decreasing ramps also superimposed after the yielding point. This confirms the non-thixotropic behavior of the gels used in the experiments. The yield stress for each material has been calculated as the shear stress at which the maximum apparent viscosity was achieved [1], [53]. The flow curve of each fluid acquired at decreasing shear rates was fitted well by a Herschel-Bulkley (HB) model. The HB model is described as follows:

$$\dot{\gamma}_{ij} = 0 \qquad \|\tau\| \leq \tau_y \tag{3.5}$$

$$\tau_{ij} = \left[K \|\dot{\gamma}\|^{n-1} + \frac{\tau_y}{\|\dot{\gamma}\|}\right]\dot{\gamma}_{ij} \qquad \|\tau\| > \tau_y$$

where *K* is the consistency factor, *n* is the shear thinning index and τ_y is the yield stress. τ_{ij} is the deviatoric stress and $\dot{\gamma}_{ij}$ is the strain rate tensor. $\|\tau\| = \sqrt{\sum_{ij} \frac{1}{2} \tau_{ij}^{\ 2}}$ and $\|\dot{\gamma}\| = \sqrt{\sum_{ij} \frac{1}{2} \dot{\gamma}_{ij}^{\ 2}}$ are the second invariants of the stress tensor and strain rate tensor respectively [1], [54]. The fitted HB-parameters of the gels used in the tests are reported in Table 3.1. The yield stress and apparent viscosity of the water-based gels increased by increasing the concentration. The comparison between data obtained for glycerol-solution-based and water-based 0.1% gels reveals that elevating the viscosity of the solvent does not lead to a noticeable change in the rheological properties of the samples. Another point that needs to be emphasized regarding the data in Figure 3.1, is the significant decrease of the yield stress of highly sheared 0.1% carbopol gel. The effect of the preparation protocol and mixing rate on the rheological behavior of carbopol gels were studied before by Geraud et al. [52] and was found that stirring the gel at a high rate would lead to significant modification of its microstructure and breakage of the microgels to smaller units.

In addition to the time dependency associated with the fluid itself, another source of uncertainty due to time dependency could originate from the experimental setup, which could lead to erroneous measurements of the viscometric and velocimetric properties of the flow. Therefore, a time dependent experiment to investigate the dynamic response of the system was performed.

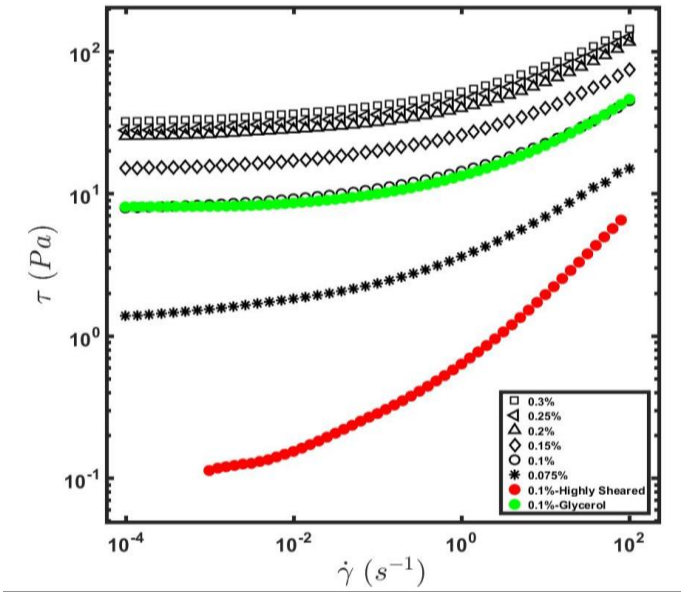

Figure 3.1) Flow curves of various concentrations of carbopols used in the experiments obtained with a rotational rheometer. Data for shear rates below 10^{-3} s^{-1} was not collected for highly sheared 0.1% carbopol gel due to its reduced viscosity.

Figure 3.2 represents the flow curve measured during a time dependent flow rate test for 0.075% carbopol gel. As shown in the inset of this figure, the sample was sheared over ramp up and ramp down flow rate tests with a time step of 60 s. The shear stress corresponding to each flow rate was calculated by averaging the measured wall shear stresses over time.

The data corresponding to the ramp up test followed those obtained during the ramp down test very well. Slight discrepancies are observed below the yield stress which are in the order of error bars of the experimental measurements.

Table 3.1) Rheological properties of carbopols used in the experiments.

Concentration $(wt/wt\ \%)$	τ_y (Pa)	K $(Pa.s^n)$	n
0.075	1.41	2.22	0.40
0.1	8.11	6.03	0.39
0.15	15.08	10.60	0.37
0.2	25.76	13.98	0.40
0.25	28.13	17.38	0.37
0.3	32.36	19.82	0.37
0.1 - Highly Sheared	0.12	0.44	0.61
0.1 - 31% Glycerol	8.00	5.16	0.43

Totally, it can be concluded from the results demonstrated in Figure 3.2, that the steady shear stress measured at each step is not influenced by the time and the intensity of pre-shearing, shear history, or any other source of time dependency related to the rheology of the fluid or response time of the experimental setup at time scales in the order of the measurements. It in turn guarantees the repeatability of the experiments and measurements. It should be noted that in the results presented in the next sections of this chapter, each flow rate was given two minutes to reach the steady-state condition before starting the measurements. This indicates that all the measurements were conducted when the steady flow was established in the capillary tube.

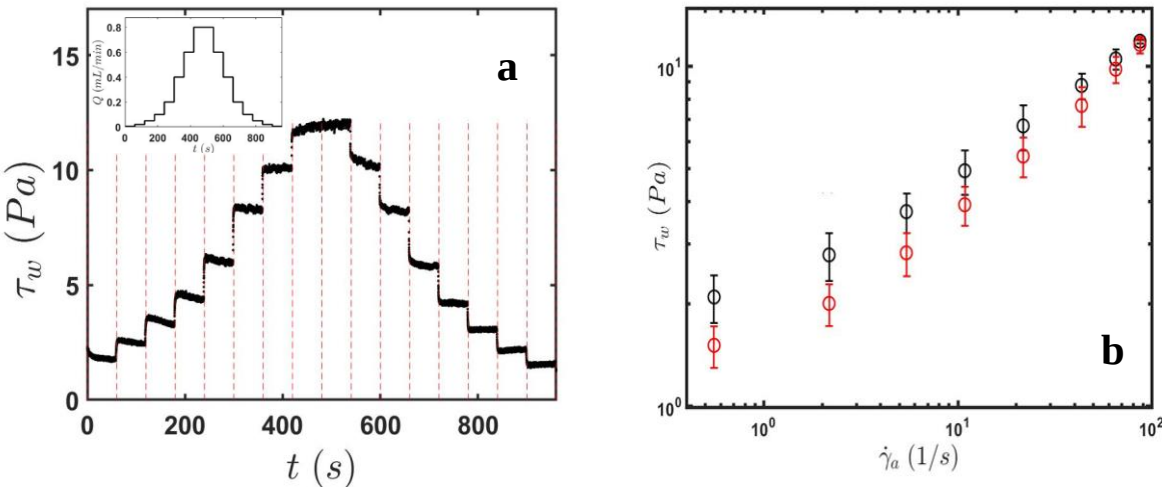

Figure 3.2) (a) Wall shear stress corresponding to the variation of the flow rate with time (see inset) for 0.075% carbopol gel. (b) Carbopol 0.075% flow curves obtained during ramp up and ramp down tests presented in black and red, respectively.

3.2.3 Experimental Method

In order to find the flow curve of carbopols using the viscometry unit, first, the fluids were pre-sheared at a flow rate of 2 mL/min for 60 s and the experiments were conducted from the highest flow rate (2 mL/min) to the lowest (0.001 mL/min) to avoid the elastic strain of the materials at lower shear rates [1].

To find the velocity profiles using the flow visualization unit, first, the capillary tube was filled with the fluid. The OCT was then focused on the centerline of the capillary tube. Fluids were pre-sheared at a flow rate of 2 mL/min for 60 s and the flow visualizations were conducted from the highest flow rate (0.3 mL/min) to the lowest (0.001 mL/min). Each flow rate was given 60 s to reach steady-state before recording.

3.2.4 Results

Capillary flow curves of carbopol gels are displayed in Figure 3.3a. The salient feature of these flow curves is their linear behavior below the yielding point (see Figure 3.3b). Non-linearity of the flow curves over the yielding point is attributed to the shear thinning behavior of the fluids. Flow visualization results confirm that the linear region corresponds to the fully plug flow (blue curve in Figure 3.4). This can be interpreted as the lubrication of carbopol microgels over a thin layer of a Newtonian fluid on the wall. Above the yielding point, flow is due to both deformation and slip (black curve in Figure 3.4). Slip behavior of the fluid below the yield stress contradicts the common belief of the yielding threshold for the onset of motion of fluid along the capillary. The question raised here is that whether there is a sliding threshold for the onset of the flow. Seth et al. [9] proved the presence of sliding yield stress in the steady torsional flow and related it to the attractive forces between soft particles and shearing surfaces.

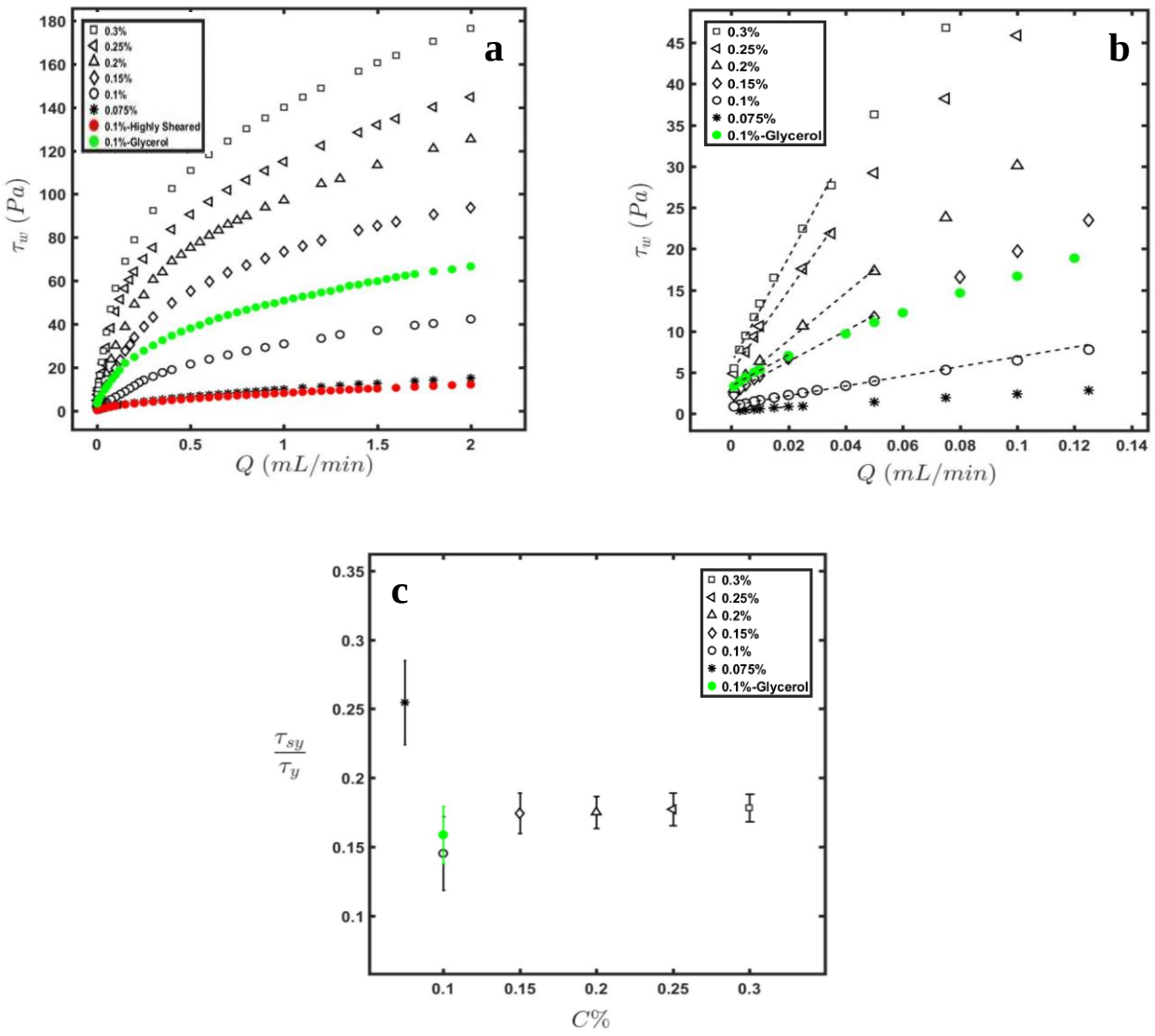

Figure 3.3) a) Wall shear stress versus flow rate for capillary flow of carbopol gels with various concentrations. The data corresponding to the highly sheared 0.1% carbopol and glycerol-solution-based 0.1% carbopol are shown in red and green, respectively. For all the cases except for highly sheared 0.1% carbopol, both the linear regime before the yielding and non-linear shear thinning regime after the yielding is observed. b) Enlarged linear region for carbopol solutions. The dashed lines are fitted lines on the data in the linear region ($\tau_{sy} < \tau_y$). c) Normalized sliding yield stress with respect to the concentration of carbopol gels. Here, the value of the sliding yield stress obtained for glycerol-solution-based carbopol was scaled by the viscosity ratio of its solvent (glycerol solution) and water, i.e. μ_s/μ_w.

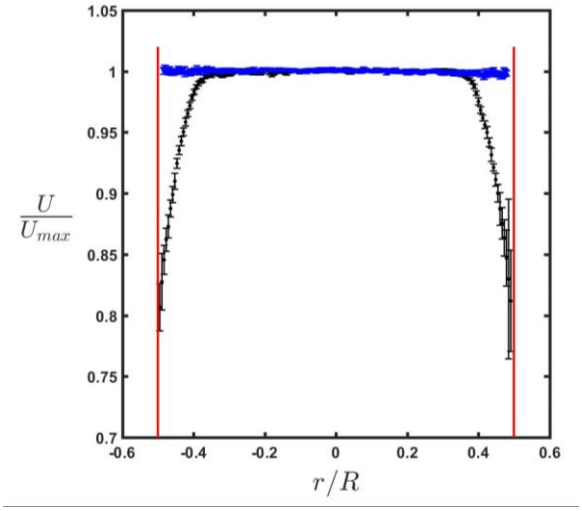

Figure 3.4) Sample velocity profiles of 0.075% carbopol gel. Fully plug regime at $Q = 0.02\ mL/min, \frac{\tau_w}{\tau_y} = 0.6$ shown in blue. Yielded regime at $Q = 0.1\ mL/min, \frac{\tau_w}{\tau_y} = 1.7$ shown in black. The red lines indicate the wall position.

In this study, the sliding threshold was estimated by linear extrapolation of the linear region of the flow curves below the yielding point to the zero flow rate. Results are presented in Figure 3.3b, c. As illustrated in these figures, for water-based carbopol with concentrations greater than 0.1%, the sliding threshold was found to change linearly by the yield stress,

$$\tau_{sy} = (0.18 \pm 0.01)\tau_y \tag{3.6}$$

Increasing the viscosity of the solvent fluid would lead to the increase in the sliding yield stress by the same ratio. As indicated in Figure 3.3c, the sliding yield stress of glycerol-solution-based carbopol gel scaled by the viscosity ratio of its solvent and water (i.e. $\mu_s/\mu_w = \frac{0.0027}{0.001} = 2.7$), follows the linear correlation obtained for the water-based carbopol gels.

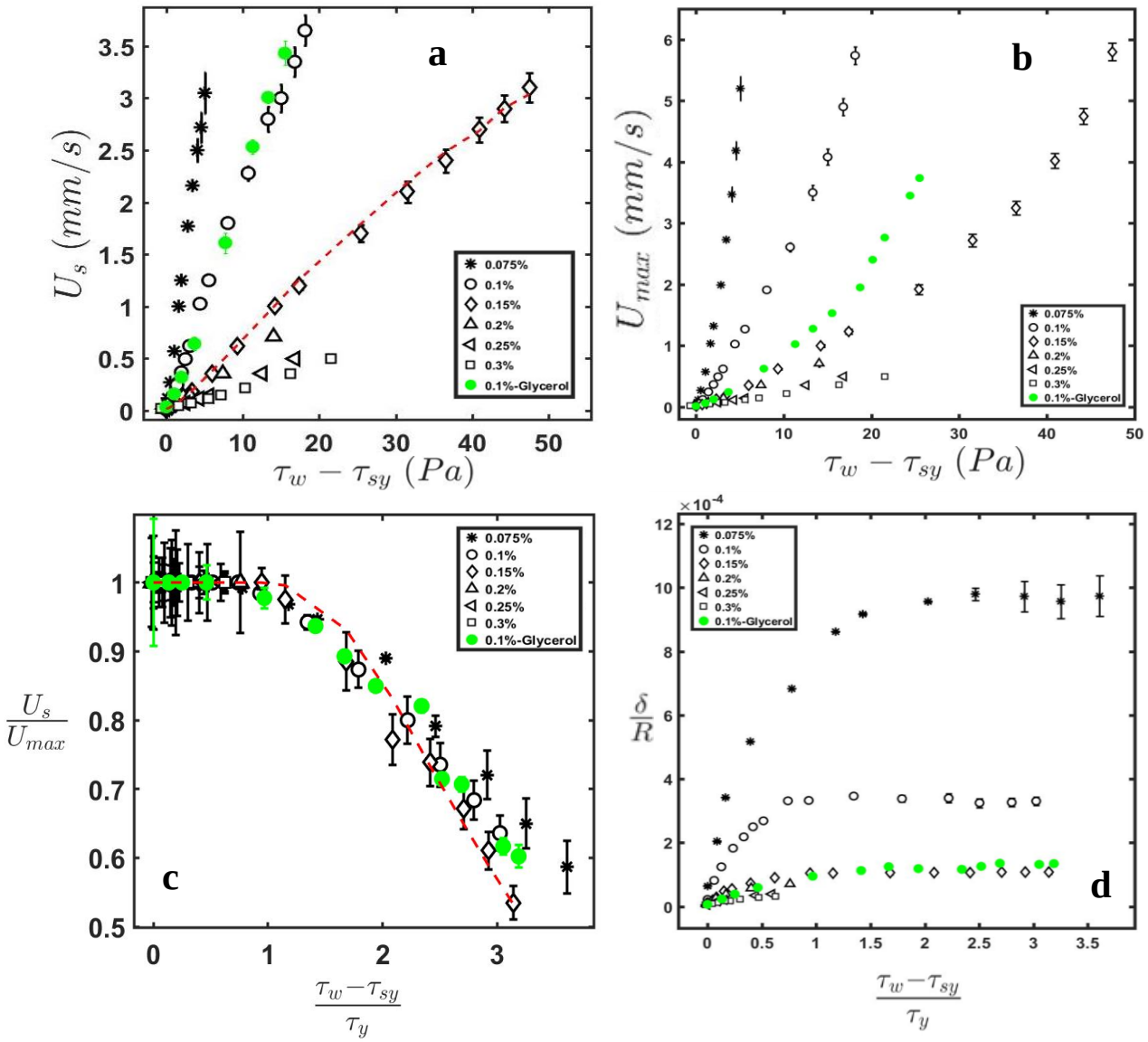

Figure 3.5) Variation of (a) the slip velocity with the excess shear stress. Scaled glycerol-solution-based 0.1% carbopol data with the solvent viscosity ratio superimposes data of water-based carbopol 0.1%, (b) the maximum velocity (plug velocity) with the excess shear stress, (c) the normalized slip velocity with the normalized excess shear stress, and (d) the normalized thickness of the slip layer with the normalized excess shear stress. Slip velocity measurements above the yielding point were not possible for carbopol concentrations above 0.15% due to the high flow rates required to reach the deformation region, which are above the limits of the flow visualization unit. The red dashed curves represent the analytical data for 0.15% carbopol gel (◊) obtained from Equation 3.7 and using the rheological properties stated in Table 3.1

The slip velocity and maximum velocity (plug velocity) of carbopol gels at different excess wall shear stresses, $(\tau_w - \tau_{sy})$, are presented in Figures 3.5a and 3.5b respectively. The normalized slip velocity and normalized thickness of the slip layer with respect to the normalized excess wall shear stresses are also indicated in Figures 3.5c and 3.5d respectively. For each carbopol gel, the wall slip velocity increases along with the wall shear stress, in both regions below and above the yield stress. However, the contribution of the slip flow rate to the total flow rate decreases by increasing the shear stress over the yielding point (see Figure 3.5c). The thickness of the apparent slip layer could be calculated by $\delta = \mu_s \frac{U_s}{\tau_w}$, under isothermal and laminar conditions and by assuming that it contains a particle depleted, fully developed, Newtonian and incompressible layer of solvent fluid. The results of the slip layer thickness are shown in Figure 3.5d. For each carbopol gel, the slip layer thickens by increasing the wall shear stress until it reaches a plateau. The wall slip velocity and the thickness of the lubrication layer decrease by increasing the concentration of carbopol gel. This can be attributed to the osmotic deswelling of the carbopol microgels at higher concentrations; the higher the concentration of carbopol gel, the higher the induced osmotic pressure that pushes the soft particles against the shearing surfaces which leads to larger deformation of microgels [8], [9], [13], [56]–[58].

To assess the validity of the experimental measurements, alternatively, the wall slip can be quantified indirectly by analysing the capillary rheometry data. According to the Mooney's method [4], the slip flow rate, $\pi R^2 U_s$, can be also estimated by subtracting the imposed flow rate, Q, from the flow rate calculated by a Hershel-Bulkley based model for the fluid flow at the corresponding wall shear stress and with no-slip condition at the wall [11], [50],

$$\pi R^2 U_s = Q - \left(\frac{\tau_w}{K}\right)^{\frac{1}{n}} \frac{\pi R^3}{\left(\frac{1}{n}+1\right)} \left[\left(1 - \frac{\tau_y}{\tau_w}\right)^{\frac{1}{n}+1} - \frac{2\left(1-\frac{\tau_y}{\tau_w}\right)^{\frac{1}{n}+3}}{\left(\frac{1}{n}+3\right)} - \frac{2\left(1-\frac{\tau_y}{\tau_w}\right)^{\frac{1}{n}+2}}{\left(\frac{1}{n}+3\right)} \frac{\tau_y}{\tau_w} \right] \quad (3.7)$$

The HB parameters of the fluids, *K*, *n*, τ_y are mentioned in Table 3.1. The wall slip values estimated using Equation 3.7 are shown with a dashed curve in Figures 3.5a and 3.5c for the carbopol gel 0.15%. The agreement between the data obtained from Equation 3.7 and those obtained from the direct estimation of the wall slip using the velocity profiles confirms the assumption of a Hershel-Bulkley model for the fluid flow with the presence of wall slip.

Using data reported in Figure 3.5, it is possible to investigate the general slip models for carbopol gels. Two separate slip regimes for carbopol gels at stresses below and above the yield stress are identified. Below the yielding point, the wall slip data for water-based carbopol solutions changes by a power-law relation with respect to the excess shear stress and its slope is well represented by a function of gel concentration,

$$U_s = f(c).(\tau_w - \tau_{sy})^{1.2}, \quad f(c) = 7.42 \times 10^{-5} C^{-3.42}, \quad R^2 = 0.998 \quad (3.8)$$

Nonlinear variation of the slip velocity with the excess shear stress is consistent with the continuous increase in the slip layer thickness with the excess shear stress below the yielding point. However, Meeker et al. and Seth et al. [8], [9] predicted a quadratic form of relation between the slip velocity and the excess shear stress for wall slip behavior of carbopol gels in steady torsional flow in the unyielded regime. In the deformation regime, the slip velocity varies linearly with the excess shear stress,

$$U_s \sim (\tau_w - \tau_{sy})^{1.00 \pm 0.02}, \quad R^2 = 0.998 \quad (3.9)$$

therefore, the slip layer thickness reaches a plateau which is a function of gel concentration. The linear variation of the slip velocity with the shear stress over the yielding point is also predicted by [9] in steady torsional flow and [12], [35] in capillary flow. According to the elasto-hydrodynamic lubrication theory, the thickness of the slip layer is proportional to the deformation of soft microgels that results from interplay between osmotic pressure, hydrodynamic lubrication force and surface forces. Since the deformations of microgels are limited by their yielding strain, the thickness of the slip layer should remain constant over yielding point. Despite what was reported in the literature for the wall slip behavior of polymer melts [58], results of the slip layer thickness over the yielding point confirms the independency of carbopol gel wall slip on the normal stress or pressure in the capillary flow.

Despite the evident linear behavior of wall slip above the yielding point, fitting to the data in this region does not lead to a general linear form of equation that could be related to gel concentration. To better characterize the slip velocity data in this region, the normalized slip velocity, U_s/U_{max}, against the normalized excess shear stress, $\frac{\tau_w-\tau_{sy}}{\tau_y}$ was considered (see Figure 3.5c). As shown in this figure, below the yielding point the total flow is only due to slip, while at larger stresses the material yields and consequently the wall slip is influenced noticeably by the fluid deformation. The interesting point is that normalized wall slip data corresponding to the carbopol gels with different concentrations and solvents fall on each other in Figure 3.5c, and are well presented by,

$$\frac{U_s}{U_{max}} = 1 - (0.04 \pm 0.01).\left(\frac{\tau_w-\tau_{sy}}{\tau_y}\right)^{2\pm0.05}, \quad R^2 = 0.937 \tag{3.10}$$

A comparison between the slip velocities obtained for glycerol-solution-based and water-based carbopol gel reveals the linear dependency of the wall slip on the fluidity of the solvent, i.e. $1/\mu_s$.

As shown in Figure 3.5a, the wall slip data for glycerol-solution-based 0.1% carbopol gel scaled by the viscosity ratio of glycerol solution and water, follow those predicted for water-based 0.1% carbopol gel well. The linear relationship found between wall slip and fluidity of the solvent is in accordance with the elasto-hydrodynamic slip model and experimental results reported by Meeker et al. [8] for wall slip of microgel pastes in a steady torsional flow. They also indicated that the wall slip of microgel pastes varies by elastic modulus and radius of the soft particles, as stated in Equation 3.4.

For a known solvent, U^* in Equation 3.4 is only a function of gel concentration and stirring rate during its preparation. The higher the stirring rate, the smaller are the microgel sizes as well as the bulk elastic modulus [52]. Hence, it is interesting to compare the wall slip behavior of two gels with the same solvent and concentration that were prepared at different stirring rates. Therefore, slip measurement tests were repeated for 0.1% carbopol gel which was sheared at high stirring rate of 1200 rpm. Results of the normalized slip velocity with respect to the wall shear stress are illustrated in Figure 3.6. In accordance to what expected from Equation 3.4, a significant decrease in the wall slip is observed when comparing the results of carbopol solution prepared at high stirring rate with the results of the normal 0.1% carbopol solution prepared at stirring rate of 300 rpm.

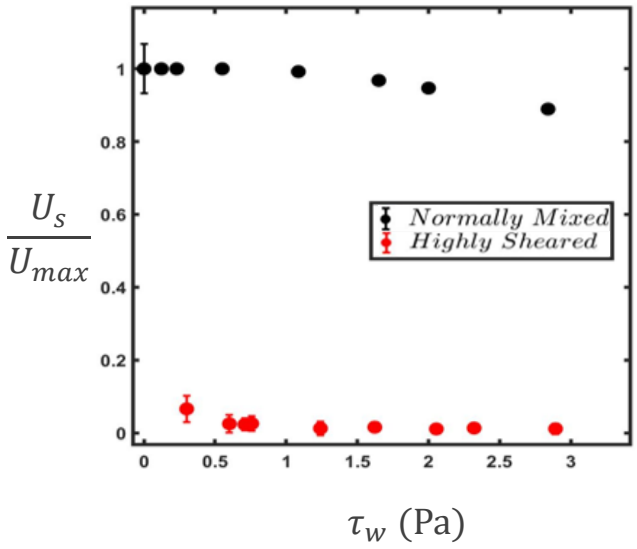

Figure 3.6) Normalized slip velocity with respect to the wall shear stress for both highly sheared and normally mixed 0.1% carbopol gels. Slip velocities are found to be much smaller compared to normally mixed carbopol gels.

3.3 Time Dependent Behavior of Laponite Suspension

In addition to the wall slip, many complex fluids show a time dependent rheological behavior based on the previous shear history, known as thixotropy. This feature is attributed to the microstructure of the material, where it starts to build-up with time at rest, known as aging, and break down while sheared, known as rejuvenation [14], [59]–[61].

One of the most important questions while dealing with thixotropic materials is when they start to flow. A major application of studying the start-up flow of thixotropic materials is in the oil and gas industry. After shutdown of the well (due to maintenance, emergency, etc.) the waxy crude oil in the pipeline starts to form a gel; therefore, restarting the flow in the pipeline can become a significant issue [17], [18]. In this section, the capability of the proposed experimental setup in

capturing the time dependent behavior of laponite suspension as a thixotropic fluid is investigated by studying the effect of thixotropy on start-up flow as well as the behavior of shear stress with step changes in the shear rate.

3.3.1 Materials

A 1.25% (wt/wt) aqueous suspension of laponite, which is often used as a model thixotropic fluid, was used in this study by first baking the laponite powder at 100°C for 4 hours to remove any moisture. The powder was given 1 day to rest before starting the preparation of the aqueous suspension. Sodium hydroxide (NaOH) and sodium chloride (NaCl) solutions were prepared in advance to be able to add exact concentrations of them to the solution. 0.04 mol/L solution of NaOH was prepared by dissolving 1.6 g NaOH in 1 L of deionized water. Similarly, 0.4 mol/L solution of NaCl was prepared by dissolving 23.4 g NaCl in 1 L of deionized water. Next, a bucket filled with 4 L of deionized water was prepared. 10.23 mL of the NaOH solution was added to the water and mixed at 300 rpm for 30 min. A pH of 10 was obtained during this process. 50 g of baked laponite was gradually added to the mixture and stirred at 300 rpm for 60 min. Next, 10 mL of the NaCl solution was added to adjust the ionic strength of the mixture. The solution was mixed at 300 rpm for 48 hours. After final preparation of the suspension, it was given 7 days rest for aging before conducting the experiments, so that the microstructures have enough time to build-up [18], [61]–[63].

Laponite suspension was prepared following the procedure described in details in [18], [64]. According to the rheological study of the laponite in [18], [64], the material shows a yield stress of 5 Pa, in addition to the thixotropic and shear thinning behaviors.

3.3.2 Experimental Method and Results

In order to perform the start-up and step shear rate experiments, first, a flow rate of 0.5 mL/min was imposed on the sample until the borosilicate glass capillary tube was completely filled with laponite suspension. Next, a resting time of 1 hour was given to the sample to restore its microstructures. A series of step flow rates were imposed on the sample (as shown in the inset of Figure 3.7) and the subsequent pressures were measured.

As demonstrated in Figure 3.7, the fluid was at rest for 1 hour until t = 10 s, where a flow rate of 0.3 ml/min was imposed on the sample. The first peak after the initial 1 hour rest time represents the start-up behavior of laponite suspension from rest to a steady-state motion. The stress required for the onset of motion is found to be 3 times larger than the stress required for the steady-state flow. The transient behavior of the shear stress (pressure) due to sudden stepwise changes in shear rate (flow rate) reflects the thixotropic behavior of the material. In a stepwise increase in shear rate, instantaneously, the microstructure size would remain the same. As the microstructure experiences the higher shear rate, it starts to disintegrate until it reaches a balance at the new shear rate, which leads to a decrease in shear stress after the initial overshoot. The same condition is true when applying a stepwise decrease in shear rate. Instantaneously, the microstructure size is again the same and the fluid is less viscous, which causes a substantial decrease in the shear stress. The microstructure then starts to build-up over time until it reaches an equilibrium, which leads to an increase in the stress after the initial undershoot [14], [59], [60]. Figure 3.7 also shows that the longer the rest time, the more structure build-up, thus, the higher the shear stress required for the flow to start-up. This can be observed by comparing the first and last peak magnitudes of this

figure. In the last step, even though the flow rate is higher than the first step (1 mL/min compared to 0.3 mL/min), the stress overshoot is less.

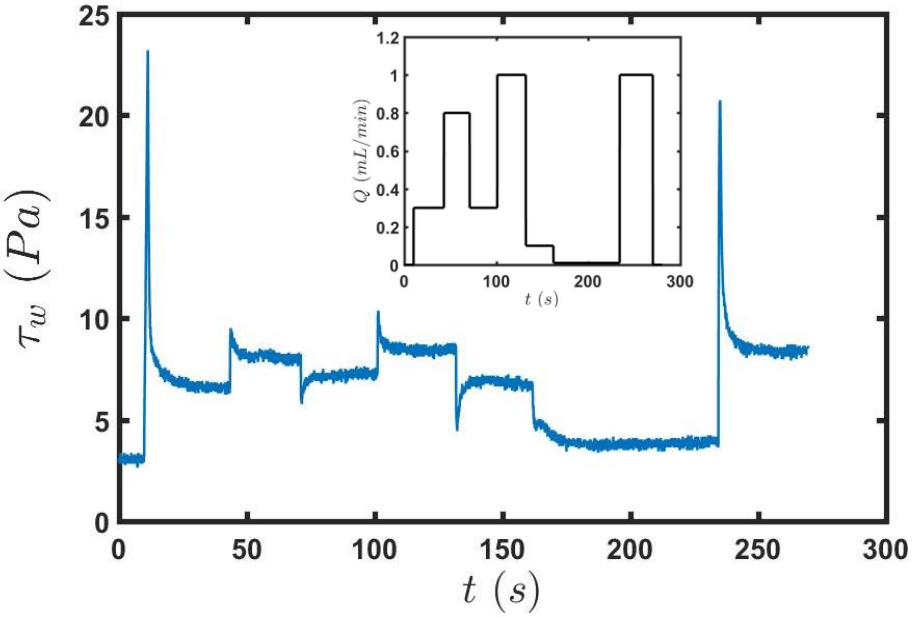

Figure 3.7) Wall shear stress variation corresponding to stepwise change in flowrate by time (see inset). The overshoots and undershoots are indicative of the thixotropic behavior of the material. This behavior was not observed in the stepwise change in flow rate test on carbopol 0.075% (shown in Figure 3.2a), which is another validation for the non-thixotropic behavior of carbopols used in this study. The value of the pressure measured by the sensor at zero flow rate can be associated to the residual stresses remained in the fluid after the cessation of the flow.

3.4 Conclusions

In the first section of this chapter, the slip behavior of carbopol gels in a pressure driven flow was investigated by utilizing high resolution imaging of their flows in a glass capillary tube. The viscometric unit of the experimental setup was used to find the capillary flow curves of the carbopols. Fully plug flow was observed by the velocimetric measurements, when the wall shear stress was below the yield stress. The linear behavior of the capillary flow curve in this region proved the lubrication of the unyielded gel by a thin layer of the Newtonian solvent. Wall slip behavior of carbopol gels in the deformation region, where the wall shear stress is above the yield stress, was also studied in this study. In addition, the sliding threshold, below which the gel sticks to the capillary wall, was found to change linearly with the yield stress. Furthermore, the findings suggest a general model to explain the wall slip of carbopol gels in Poiseuille flow. Below the yielding point, the slip velocity is linked to the excess wall shear stress by a power of 1.2, while it varies linearly with the excess wall shear stress above the yielding point. The dependency of the wall slip velocity on the concentration of gels below the yielding point was systematically investigated as well. A series of experiments to examine the dependency of the wall slip on the viscosity of the solvent and stirring rate during preparation were performed at a fixed concentration. The results confirmed that increasing the viscosity of the solvent leads to a decrease in the wall slip. However, the form of relation between the wall slip and the excess shear stress was independent of the solvent viscosity. In addition, the carbopol solution prepared at a higher stirring rate was found to exhibit smaller slip velocities.

In the second section of this chapter, the thixotropic behavior of laponite suspension and its effect on the start-up flow was investigated. It was shown that imposing longer rest times on the material

lead to higher start-up shear stresses; thus, more pressure required for the onset of motion. Transient behavior of shear stress due to step changes in shear rate was analyzed as well. This study helps to better understand the start-up flow of waxy crude oil in a pipeline in the oil and gas industry.

Results of this chapter validate the capability of the proposed experimental setup in capturing complex fluid flow behaviors such as wall slip and time dependency. Studying the former would not have been possible using a conventional rotational rheometer due to lack of a flow visualization unit. Studying the latter with a capillary rheometer would be more reasonable due to its geometrical similarity with the flow in a pipeline.

Chapter 4:

Biofluids

4.1 Introduction

In this chapter, synovial fluid, as an example of a non-Newtonian biofluid, was chosen to assess the capability of the proposed capillary rheometry method in capturing the rheological behavior of biofluids. Synovial fluid analysis is a crucial step in the diagnosis of joint diseases. One way to determine the presence of arthritis (e.g. osteoarthritis, rheumatoid arthritis, etc.) is by analyzing the rheological characteristics of the synovial fluid sample and comparing it to the data of a healthy synovial fluid. The main focus of this study is on the synovial fluid of the knee joint. Rotational rheometers have been the widely used instrument for these analyses; however, they are not capable of simulating the actual condition experienced by the synovial fluid in the joints. Range of shear rates that occur in the knee joint can exceed 10^5 s^{-1} while running [20], [21]; however, due to inertial instabilities it is not feasible to achieve shear rates above 1000 s^{-1} using rotational rheometers. In addition, they expose the fluid to the surrounding environment which could lead to evaporation and contamination of the samples, and are expensive [5]. In this chapter, a general overview of synovial fluid and its rheological properties is presented. The efficacy of the proposed method is investigated by comparing the rheological data of osteoarthritic synovial fluids using both rotational and capillary rheometry methods.

4.2 Synovial Fluid

Synovial fluid provides the necessary lubrication and shock absorption in synovial joints. It supplies nutrition to the articular cartilage, since cartilage lacks any blood vessels or lymph [65]. Synovial fluid is produced by synovium (synovial membrane) which is the tissue that surrounds the joint [65]. It is comprised primarily of hyaluronic acid (HA), lubricin, γ-globulin, albumin, lipids, cholesterol and water [19], [66]. The rheological characteristics of synovial fluid are mainly attributed to the hyaluronic acid [65].

The healthy knee joint normally contains up to 4 mL of synovial fluid. Normal synovial fluid is colorless and clear. Other appearances may indicate various diseases. Thus, physical and chemical analyses, alongside the rheological analysis of synovial fluid provide a good understanding in the diagnosis of joint diseases [67].

4.3 Synovial Fluid Pathology

Arthritis is one of the major causes of disability worldwide. Arthritis is generally referred to any kind of joint pain or disease. There are in fact more than 100 different types of arthritis. 20% of the population in North America (1 in every 4) are diagnosed with arthritis. Common arthritis joint symptoms include swelling, pain, stiffness and decreased range of motion [68], [69]. Osteoarthritis (OA) as the most prevalent type of arthritis is chosen to be studied in this research.

4.3.1 Osteoarthritis

Osteoarthritis (OA) is the most common type of arthritis. OA is a painful degenerative joint condition that affects 630 million people worldwide (15% of world population) [70], [71]. In north America, OA affects approximately 34% of people over 65 years of age (more than 21 million) and costs the North American economy approximately US$60 billion annually. Thus, it is becoming a major medical and financial concern [69], [72].

In synovial joints, synovial fluid and articular cartilage both contribute to joint lubrication. Articular cartilage is the rubbery material which covers the ends of each bone. It allows the joints to smoothly move against each other. In OA, the cartilage gradually wears away which leads to pain, swelling and difficulty in the joint motion. In the severe cases, the bones rub against each other, causing more pain and immobility [21], [68], [73], [74].

Unfortunately, there has not been any proven treatment developed for OA so far. Current therapeutic approaches for OA mainly search for alleviating the pain and symptoms associated with this disease rather than impeding its progression. In severe cases of OA, the patient might be recommended for total knee arthroplasty (TKA), in which the joint will be replaced with prostheses [75], [76]. Viscosupplementation has been introduced as an emerging method for OA treatment recently. In this method, an intra-articular injection of a lubricating fluid with resembling rheological properties to healthy synovial fluid has shown to improve joint mobility by restoring the rheological and physiological properties of the degrading synovial fluid. However, more systematic evaluation of the viscosupplements is required to support the efficacy of this method [73], [74], [77]. Therefore, it is of utmost importance to prevent the occurrence of OA by

controlling the modifiable risk factors predisposing an individual to OA such as obesity, diet, joint traumatic injury and abnormal loading on joint [78], [79].

4.4 Rheological Behavior of Synovial Fluid

Synovial fluid is a non-Newtonian material; therefore, its rheological properties are of much interest. Synovial fluid mainly owes its viscoelastic properties to hyaluronic acid. In OA synovial fluid, both viscosity and elasticity are lowered due to a decrease in HA concentration and molecular weight [65], [77], [80]. Synovial fluid is shear thinning and has rheopectic behavior at low shears. The former meaning the viscosity will decrease as the shear rate increases. This behavior enables smoother motion while running. The latter means that the fluid shows a higher viscosity the longer it undergoes a shearing force. The rheopectic property of synovial fluid is attributed to the entanglement of the protein network. This behavior is useful during periods of low shear such as standing, which provides a more elastic buffer between the bones, hence, preventing them to come into contact [19], [81], [82]. OA synovial fluid viscosities differ from a healthy synovial fluid mainly at low shear rate regions. In addition, OA synovial fluids tend to have a shorter relaxation time (~ 0.1 s) in comparison to a healthy synovial fluid (~ 10 s) [65].

4.5 Methodology

Synovial fluid samples were aspirated from patients undergoing total knee arthroplasty (TKA) surgery. The operations were done at the University of British Columbia hospital. An informed consent was obtained from each patient prior to the surgery to allow for joint fluid collection in

accordance with the ethics approval obtained from the University of British Columbia Board of Ethics and the Vancouver Coastal Health Institute to study the rheological behavior of aspirated sample synovial fluids at high shears. The inclusion criteria for participation in this research were patients diagnosed with knee osteoarthritis, had age limit of 50 – 85 years and have had no surgical history on the study knee within the past 10 years. Subjects diagnosed with inflammatory arthritis (e.g. rheumatoid arthritis) were excluded from this research.

After completion of pre-surgery preparations and achieving anesthesia, approximately 2-5 mL synovial fluid was aspirated from the knee joint by a professional orthopaedic surgeon prior to the initial incision. This process does not have any effect on the operation and would not lengthen the time of the surgery. Furthermore, there would not be any additional pain or discomfort associated with this process.

Synovial fluid samples were collected in glass vials and were frozen at temperature of -20 °C. Experiments using both rotational and capillary rheometers were done within one week of aspiration. Not all the aspirated synovial fluids were suitable for rheological measurements as some of them were very low in volume or were mixed with blood. Among the aspirated synovial fluids, two samples were suitable for rheological analysis, both having a volume of approximately 3 mL. Results obtained from the two samples are presented in the following section.

4.6 Viscometric Analysis of Synovial Fluid

In order to observe the behavior of synovial fluids at high shear rates, viscometry unit, demonstrated in Figure 2.1, with the high aspect ratio stainless-steel tube (diameter of 0.254 mm

and length of 914.4 mm) was used. The internal volume of the capillary tube is 0.046 mL, therefore, only a small fraction of the total sample volume (3 mL) would be consumed for filling the tube. In capillary rheometry, to remove any loading effects or shear history, sample fluids were driven and pre-sheared inside the tube using the syringe pump at a flow rate of 1 ml/min until the tube was filled with the fluid. The fluids were given 1 minute rest before the actual experiment. Considering the sample volumes, flow rates in the range of 4 ml/min down to 0.01 ml/min were imposed on the fluids to achieve wide range of shear rates. Capillary rheometry experiments were conducted at room temperature (25 °C). After completion of each test, additional cleaning protocol needed to be performed to avoid any biohazard safety concerns. 1% concentration of Tergazyme solution (Alconox) was prepared by dissolving its powder in hot water. The experimental setup was then cleaned by first circulating Tergazyme solution for several times inside the capillary tube and pressure sensor. Water and isopropyl alcohol were respectively circulated through the experimental setup afterwards, followed by drying with compressed air.

To validate the data obtained from the capillary rheometer, results were compared with the data obtained from Malvern Kinexus rotational rheometer with a 4° angle, 40 mm diameter cone and plate geometry. In rotational rheometry, similarly, to remove any loading effects or shear history, samples were pre-sheared at shear rate of 50 s^{-1} for 30 s followed by a 1 minute rest. A table of shear rates in the range of 10^{3} to 10^{-2} were applied on the samples and the subsequent stresses were measured. It is worth mentioning that descending shear rates were applied on the samples to avoid any possible elastic strain at lower shear rates [1].

Figure 4.1 demonstrates the variation of viscosity with shear rate for both synovial fluid samples using the two capillary and rotational rheometry methods. Results obtained from both methods are

found to be in good agreement with each other. It should be emphasized that shear rates above 1000 s^{-1} were not possible to achieve using rotational rheometry due to low sample viscosity and inertial instabilities [5], [21]. Shear rates as high as 7000 s^{-1} were obtained by the capillary rheometer. Even higher values of shear rate would have been feasible to achieve, given more sample volumes were available. A power-law behavior in the range of 10 - 10^4 s^{-1} was observed for both samples. The different behavior observed in the range of 10^{-2} - 10 s^{-1} can be due to the Carreau-Yasuda behavior of the samples. In order to reduce the uncertainty of the measurements, the experiments on each synovial fluid sample was performed twice in both the capillary and rotational rheometers and the results of the repeated tests were found to superimpose in each case.

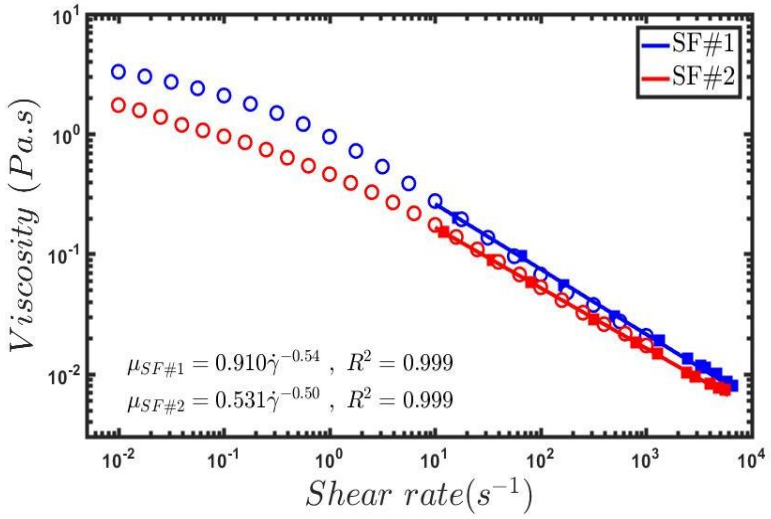

Figure 4.1) Viscosity as a function of shear rate at temperature of 25 °C. Data pertaining to the first synovial fluid sample (SF#1) are shown in blue and the second sample are shown in red. Hollow circular markers represent data obtained from the rotational rheometry and filled square markers represent the data obtained from capillary rheometry. Data obtained from the capillary rheometer follows a power-law model. Inset indicates the power-law relationships. Due to the large length of the capillary tube, error bars are so minor to be seen.

Despite having advantages such as reaching high shear rates, preventing sample evaporation and contamination, the proposed method has the limitation of experimenting in different temperatures. Temperature of synovial fluid is highly dependent on the surrounding environment temperature and physical activity, thus, neither room temperature (25 °C) nor physiological temperature (37 °C) represent the true temperature inside the joint [66].

Variation of the viscosity of the synovial fluid samples with the temperature was investigated using the rotational rheometer. As illustrated in Figure 4.2, an inverse relationship between the viscosity and temperature of the samples at a constant shear rate was found. By increasing the temperature, synovial fluid proteins will unfold, and the viscosity will decrease. They will fold back again as temperature decreases [66].

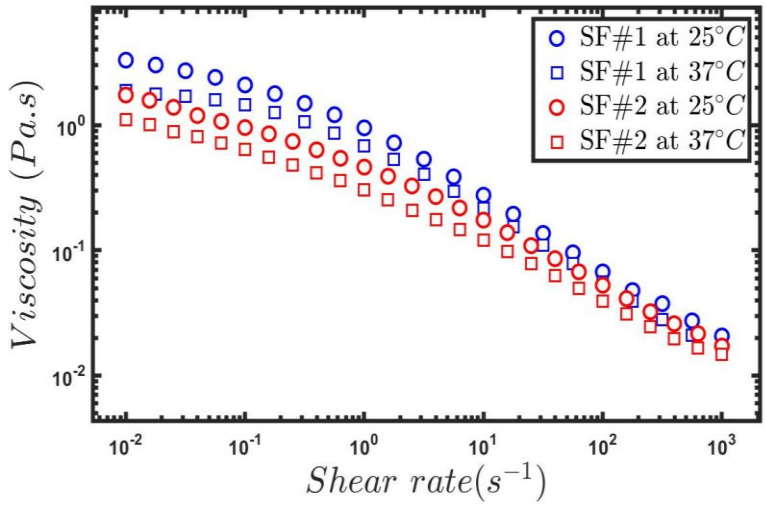

Figure 4.2) Viscosity as a function of shear rate at temperatures of 25 °C and 37 °C obtained from the rotational rheometer.

4.7 Conclusions

To determine the efficacy of the proposed capillary rheometer of this study in dealing with a variety of complex fluids, including biofluids, synovial fluid as a representative of biofluids was chosen due to its interesting non-Newtonian behavior, as well as the current literature gap in analyzing the rheological behavior of synovial fluid at high shear rates, which frequently occurs inside the knee joints. Viscometry tests were conducted on two osteoarthritic synovial fluid samples using both capillary and rotational rheometry methods. Results were shown to be in good agreement. In addition, shear rates seven times greater than the shear rate limit measurable by the conventional rotational rheometers were achieved using the capillary rheometer. Similar viscosity behavior in the range of $10^3 - 10^4\ s^{-1}$ was obtained compared to the range of $10 - 10^3\ s^{-1}$. Different behavior between the ranges of $10^{-2} - 10\ s^{-1}$ and $10 - 10^4\ s^{-1}$ is conjectured to be due to the Carreau-Yasuda behavior of the samples. In general, the proposed method offers a promising outlook on the synovial fluid research in terms of providing conditions that better resemble the one inside the joints. This could lead to further understanding of the role of synovial fluid in joint lubrication and be useful as a diagnostic aid for OA. However, more work needs to be done to be able to control the fluid temperature in the experiments, necessary for biofluids research.

Chapter 5: Conclusions

5.1 Summary and Contributions

Rotational rheometers have been the main tool for rheological analysis of complex fluids so far, due to their high precision, compatibility with wide range of material viscosities, ability to test at different temperatures, robustness, real-time measurements, etc. However, in certain cases, studying complex fluid behaviors will result in erroneous measurements or would not be feasible using a conventional rotational rheometry method. These cases usually arise when the material shows wall slip or shear banding behaviors, or while dealing with biofluids. This study addressed the shortcomings of the conventional rotational rheometry by developing a novel Rheo-PTV method that incorporates both capillary rheometry and flow visualization units. The proposed experimental setup was successfully benchmarked with both Newtonian and shear thinning fluids of known properties. Slip behavior of carbopol as a simple yield stress fluid, start-up flow of laponite as a thixotropic yield stress fluid, along with high shear analysis of synovial fluid as a biofluid were then investigated as case studies that would be challenging to investigate using a conventional rotational rheometry method. The contributions of the proposed Rheo-PTV method in each case study could be summarized as follows:

1. In the internal flow study of carbopol as a simple yield stress fluid, the fully plug flow observed at stresses below the yield stress was found to be caused by the Newtonian solvent layer. The sliding threshold, stress above which the fluid starts to flow, was also found to

behave linearly with the yield stress. A general model for wall slip as a function of wall shear stress, independent of the concentration and solvent viscosity, was developed as well. It was found that increasing the concentration, solvent viscosity and mixing rate will lead to a decrease in the wall slip. Studying the slip behavior of complex fluids was made possible by the flow visualization unit.

2. In the internal flow study of laponite as a thixotropic yield stress fluid, the effect of thixotropy on start-up flow problem was investigated. It was shown that the longer the rest time, the more structure build up, therefore, the harder would be to restart the motion of the fluid. The transient behavior of the shear stress due to step changes in the shear rate were captured as well. This case study proves the capability of the experimental setup to study the time dependent behavior of thixotropic fluids.
3. Synovial fluid of patients diagnosed with osteoarthritis as an example of biofluids were tested to analyze their behavior at high shear rates, which typically occur in joints while having high physical activities. In this study, viscometry test at shear rates up to 7000 s^{-1} was performed. A power-law behavior from 10 - 10^4 s^{-1} was observed for both samples. The different behavior observed from 10^{-2} - 10 s^{-1} is conjectured to be due to the Carreau-Yasuda behavior of the samples. This case study proves the capability of the experimental setup to investigate the behavior of biofluids at high shears, which could be useful as a diagnostic aid for various diseases.

Overall, results obtained from the above case studies confirm that the Rheo-PTV tool developed in this study has the potential to study complex fluid behaviors that are challenging to study using the conventional rheometry methods.

5.2 Limitations and Future Directions

Although the Rheo-PTV device developed in this study was shown to be capable of performing rheological analysis on complex fluids; however, there were some limitations associated with the experimental setup that are described in the following:

- Velocity profile measurements above the yield stress were not possible for high concentrations of carbopol, since the flow visualization unit was not capable of capturing the motion of the tracer particles at such high flow rates.
- Measuring the rheological characteristics of complex fluids at low shear rates was not possible with the current experimental setup, due to the limited lower bound operating range of the pressure sensors.
- It is crucial to be able to control the temperature of the material while dealing with biofluids to better resemble the physiological body conditions. The experimental setup of this study was limited to experiments at room temperature.

The results obtained in this study were sample case studies and can be further improved or extended to other type of fluids or applications. Areas in which more work could be done is listed as follows:

- Effect of rheological properties of the solvent and preparation procedures on the wall slip of carbopol microgels could be studied more systematically.
- Effect of the surface roughness of the wall on the slip behavior of complex fluids is an area that is still under question in the literature and can be further studied.

- The experiment performed on a thixotropic material in this study was a pilot study to assess the capability of the developed method in dealing with time dependent materials. Performing dynamic rheometry tests in order to find the elastic and loss moduli as well as the relaxation time using a capillary rheometer is an area that could be investigated more.
- The mechanism of slip of laponite suspension could be systematically studied as well.
- It would not be possible to make any statistical inferences on the behavior of synovial fluid at high shear rates with the two samples studied in this research. Therefore, synovial fluid samples of more patients should to be collected to obtain a more conclusive result.
- Similar to synovial fluid, blood also experiences high range of shear rates while circulating through the cardiovascular system. In addition, capillary rheometry better resembles the flow inside the vessels. Therefore, rheological characteristic of blood would be of interest as a next step.

Bibliography

[1] N. J. Balmforth, I. A. Frigaard, and G. Ovarlez, "Yielding to Stress: Recent Developments in Viscoplastic Fluid Mechanics," *Annu. Rev. Fluid Mech.*, vol. 46, no. 1, pp. 121–146, 2014.

[2] N. Kojic, J. Bico, C. Clasen, and G. H. McKinley, "Ex vivo rheology of spider silk," *J. Exp. Biol.*, vol. 209, no. 21, pp. 4355–4362, 2006.

[3] Christopher W. Macosko, *Rheology: Principles, Measurements and Applications*, vol. 86, no. 3. Wiley-VCH, 1994.

[4] F. Morrison, *Understanding Rheology*. Oxford University Press, 2001.

[5] S. Gupta, W. S. Wang, and S. A. Vanapalli, "Microfluidic viscometers for shear rheology of complex fluids and biofluids," *Biomicrofluidics*, vol. 10, no. 4, 2016.

[6] A. Magnin and J. M. Piau, "Shear rheometry of fluids with a yield stress," *J. Non-Newtonian Fluid Mech.*, vol. 23, no. C, pp. 91–106, 1987.

[7] A. Magnin and J. M. Piau, "Cone-and-Plate Rheometry Study of an Aqueous Gel of Yield Stress Fluids. Study of an aqueous gel," *J. Non-Newtonian Fluid Mech.*, vol. 36, pp. 85–108, 1990.

[8] S. P. Meeker, R. T. Bonnecaze, and M. Cloitre, "Slip and flow in soft particle pastes," *Phys. Rev. Lett.*, vol. 92, no. 19, pp. 1–4, 2004.

[9] J. R. Seth, C. Locatelli-Champagne, F. Monti, R. T. Bonnecaze, and M. Cloitre, "How do soft particle glasses yield and flow near solid surfaces?," *Soft Matter*, vol. 8, no. 1, pp. 140–148, 2012.

[10] J. Pérez-gonzález, B. M. Marín-santibáñez, Francisco Rodriguez-Gonzalez, and J. G. G.-Santos, *Rheo-Particle Image Velocimetry for the Analysis of the Flow of Polymer Melts*. InTech, 2012.

[11] S. Aktas, D. M. Kalyon, B. M. Marín-Santibáñez, and J. Pérez-González, "Shear viscosity and wall slip behavior of a viscoplastic hydrogel," *J. Rheol.*, vol. 58, no. 2, pp. 513–535, 2014.

[12] A. Poumaere, M. Moyers-González, C. Castelain, and T. Burghelea, "Unsteady laminar flows of a carbopol® gel in the presence of wall slip," *J. Non-Newtonian Fluid Mech.*, vol. 205, pp. 28–40, 2014.

[13] S. G. Hatzikiriakos, "Slip mechanisms in complex fluid flows," *Soft Matter*, vol. 11, no. 40, pp. 7851–7856, 2015.

[14] G. Ovarlez and S. Hormozi, *Lectures on Visco-Plastic Fluid Mechanics*. Springer International Publishing, 2019.

[15] T. Sochi, "Slip at fluid-solid interface," *Polym. Rev.*, vol. 51, no. 4, pp. 309–340, 2011.

[16] D. R. Hewitt, M. Daneshi, N. J. Balmforth, and D. M. Martinez, "Obstructed and channelized viscoplastic flow in a Hele-Shaw cell," *J. Fluid Mech.*, vol. 790, pp. 173–204, 2016.

[17] I. Frigaard, G. Vinay, and A. Wachs, "Compressible displacement of waxy crude oils in long pipeline startup flows," *J. Non-Newtonian Fluid Mech.*, vol. 147, no. 1–2, pp. 45–64, 2007.

[18] G. V. L. Moisés, "Effects of yield stress and thixotropy in non-Newtonian isodense displacement," PhD thesis, Pontifícia Universidade Católica do Rio de Janeiro, 2016.

[19] M. B. Chernos, "A rheological study of treatments for osteoarthritis," Master's thesis,

University of British Columbia, 2016.

[20] Z. M. Jin, D. Dowson, and J. Fisher, “Analysis of fluid film lubrication in artificial hip joint replacements with surfaces of high elastic modulus,” *Proc. Inst. Mech. Eng. Part H J. Eng. Med.*, vol. 211, no. 3, pp. 247–256, 1997.

[21] A. Madkhali, M. Chernos, D. Grecov, and E. Kwok, “Osteoarthritic synovial fluid rheology and correlations with protein concentration,” *Biorheology*, vol. 53, no. 3–4, pp. 111–122, 2016.

[22] S. Haavisto, J. Salmela, and A. Koponen, “Accurate velocity measurements of boundary - layer flows using Doppler optical coherence tomography,” *Exp. Fluids*, pp. 2–7, 2015.

[23] W. Drexler and J. G. Fujimoto, *Optical coherence tomography, Technology and Applications*. Springer, 2008.

[24] A. Buchsbaum *et al.*, “Optical coherence tomography based particle image velocimetry (OCT-PIV) of polymer flows,” *Opt. Lasers Eng.*, vol. 69, pp. 40–48, 2015.

[25] S. Jonas, D. Bhattacharya, M. K. Khokha, and M. A. Choma, “Microfluidic characterization of cilia-driven fluid flow using optical coherence tomography-based particle tracking velocimetry,” *Biomed. Opt. Express*, vol. 2, no. 7, p. 2022, 2011.

[26] M. Jalaal, C. Seyfert, B. Stoeber, and N. J. Balmforth, “Gel-controlled droplet spreading,” *J. Fluid Mech.*, vol. 837, pp. 115–128, 2018.

[27] M. Jalaal, “Controlled Spreading of Complex Droplets,” PhD thesis, University of British Columbia, 2016.

[28] R. D. Keane, R. J. Adrian, and Y. Zhang, “Super-resolution particle imaging velocimetry,” *Meas. Sci. Technol.*, vol. 6, no. 6, pp. 754–768, 1995.

[29] F. Scarano and M. L. Riethmuller, “Advances in iterative multigrid PIV image processing,”

Exp. Fluids, vol. 29, no. 7, pp. S051–S060, 2000.

[30] N.-T. Nguyen and S. T. Wereley, *Fundamentals and Applications of Microfluidics*. Artech House, 2002.

[31] C. J. Pipe, T. S. Majmudar, and G. H. McKinley, "High shear rate viscometry," *Rheol. Acta*, vol. 47, no. 5–6, pp. 621–642, 2008.

[32] R. J. Adrian, "Particle-Imaging Techniques for Experimental Fluid Mechanics," *Annu. Rev. Fluid Mech.*, vol. 23, no. 1, pp. 261–304, 1991.

[33] M. Raffel, C. E. Willert, F. Scarano, C. J. Kähler, S. T. Wereley, and J. Kompenhans, *Particle Image Velocimetry: A Practical Guide*. Springer, 2018.

[34] D. Sinton, "Microscale flow visualization," *Microfluidics and Nanofluidics*, vol. 1, no. 1. pp. 2–21, 2004.

[35] J. Pérez-González, Juan Javier López-Durán, Benjamín M. Marín-Santibáñez, and Francisco Rodríguez-González, "Rheo-PIV of a yield-stress fluid in a capillary with slip at the wall," *Rheol Acta*, vol. 51, no. 11–12, pp. 937–946, 2012.

[36] Y. Holenberg, O. M. Lavrenteva, U. Shavit, and A. Nir, "Particle tracking velocimetry and particle image velocimetry study of the slow motion of rough and smooth solid spheres in a yield-stress fluid," *Phys. Rev. E*, vol. 86, no. 6, pp. 1–6, 2012.

[37] W. Y. Hamad and T. Q. Hu, "Structure-process-yield interrelations in nanocrystalline cellulose extraction," *Can. J. Chem. Eng.*, vol. 88, no. 3, pp. 392–402, 2010.

[38] S. Shafiei-Sabet, W. Y. Hamad, and S. G. Hatzikiriakos, "Rheology of nanocrystalline cellulose aqueous suspensions," *Langmuir*, vol. 28, no. 49, pp. 17124–17133, 2012.

[39] S. Shafiei Sabet, "Shear Rheology of Cellulose Nanocrystal (CNC) Aqueous Suspensions," PhD Thesis, University of British Columbia, 2013.

[40] M. Miriam de Souza Lima and R. Borsali, “Rodlike Cellulose Microcrystals: Structure, Properties, and Applications,” *Macromol. Rapid Commun.*, vol. 70, no. 7, pp. 34–52, 2004.

[41] P. Coussot, “Yield stress fluid flows: A review of experimental data,” *Journal of Non-Newtonian Fluid Mechanics*, vol. 211. pp. 31–49, 2014.

[42] A. J. Liu and S. R. Nagel, “Jamming is not just cool any more,” *Nature*, vol. 396, no. 6706, pp. 21–22, 1998.

[43] V. Trappe, V. Prasad, L. Cipelletti, P. Segre, and D. Weitz, “Jamming phase diagram for atractive particles,” *Nature*, vol. 411, no. June, pp. 772–775, 2001.

[44] D. Bonn, M. M. Denn, L. Berthier, T. Divoux, and S. Manneville, “Yield Stress Materials in Soft Condensed Matter,” *Rev. Mod. Phys.*, 2017.

[45] J. M. Piau, “Carbopol gels: Elastoviscoplastic and slippery glasses made of individual swollen sponges. Meso- and macroscopic properties, constitutive equations and scaling laws,” *J. Non-Newtonian Fluid Mech.*, vol. 144, no. 1, pp. 1–29, 2007.

[46] G. Benmouffok-Benbelkacem, F. Caton, C. Baravian, and S. Skali-Lami, “Non-linear viscoelasticity and temporal behavior of typical yield stress fluids: Carbopol, Xanthan and Ketchup,” *Rheol. Acta*, vol. 49, no. 3, pp. 305–314, 2010.

[47] P. Coussot, L. Tocquer, C. Lanos, and G. Ovarlez, “Macroscopic vs. local rheology of yield stress fluids,” *J. Non-Newtonian Fluid Mech.*, vol. 158, no. 1–3, pp. 85–90, 2009.

[48] T. Divoux, D. Tamarii, C. Barentin, S. Teitel, and S. Manneville, “Yielding dynamics of a Herschel-Bulkley fluid: A critical-like fluidization behaviour,” *Soft Matter*, vol. 8, no. 15, pp. 4151–4164, 2012.

[49] V. Vand, “Viscosity of solutions and suspensions. I: Theory,” *J. Phys. Colloid Chem.*, vol. 52, no. 2, pp. 277–299, 1948.

[50] D. M. Kalyon, “Apparent slip and viscoplasticity of concentrated suspensions,” *J. Rheol.*, vol. 49, no. 3, pp. 621–640, 2005.

[51] D. M. Kalyon and S. Aktaş, “Factors Affecting the Rheology and Processability of Highly Filled Suspensions,” *Annu. Rev. Chem. Biomol. Eng.*, vol. 5, no. 1, pp. 229–254, 2014.

[52] B. Geraud, L. Bocquet, and C. Barentin, “Confined flows of a polymer microgel,” *Eur. Phys. J. E*, vol. 36, no. 3, 2013.

[53] M. Dinkgreve, J. Paredes, M. M. Denn, and D. Bonn, “On different ways of measuring ‘the’ yield stress,” *J. Non-Newtonian Fluid Mech.*, vol. 238, pp. 233–241, 2016.

[54] Evan Mitsoulis, “Flows of viscoplastic materials: Models and computations,” *Rheol. Rev.*, vol. 64, no. 1–4, pp. 135–178, 2007.

[55] R. Borrega, M. Cloitre, I. Betremieux, B. Ernst, and L. Leibler, “Concentration dependence of the low-shear viscosity of polyelectrolyte micro-networks: From hard spheres to soft microgels,” *Europhys. Lett.*, pp. 729–735, 1999.

[56] H. A. Barnes, “A review of the slip (wall depletion) of polymer solutions, emulsions and particle suspensions in viscometers: its cause, character, and cure,” *Journal of Non-Newtonian Fluid Mechanics*, vol. 56, no. 3. pp. 221–251, 1995.

[57] M. Cloitre and R. T. Bonnecaze, “A review on wall slip in high solid dispersions,” *Rheol. Acta*, vol. 56, no. 3, pp. 283–305, 2017.

[58] H. S. Tang and D. M. Kalyon, “Time-dependent tube flow of compressible suspensions subject to pressure dependent wall slip: Ramifications on development of flow instabilities,” *J. Rheol.*, vol. 52, no. 5, p. 1069, 2008.

[59] H. A. Barnes, “Thixotropy - A review,” *Journal of Non-Newtonian Fluid Mechanics*, vol. 70, no. 1–2. pp. 1–33, 1997.

[60] J. Mewis and N. J. Wagner, “Thixotropy,” *Advances in Colloid and Interface Science*, vol. 147–148, no. C. pp. 214–227, 2009.

[61] P. Coussot, H. Tabuteau, X. Chateau, L. Tocquer, and G. Ovarlez, “Aging and solid or liquid behavior in pastes,” *J. Rheol.*, vol. 50, no. 6, pp. 975–994, 2006.

[62] H. Tanaka, J. Meunier, and D. Bonn, “Nonergodic states of charged colloidal suspensions: Repulsive and attractive glasses and gels,” *Phys. Rev. E*, vol. 69, no. 3 1, pp. 1–6, 2004.

[63] S. Jatav and Y. M. Joshi, “Chemical stability of Laponite in aqueous media,” *Appl. Clay Sci.*, vol. 97–98, pp. 72–77, 2014.

[64] Y. M. Joshi, G. R. K. Reddy, A. L. Kulkarni, N. Kumar, and R. P. Chhabra, “Rheological behaviour of aqueous suspensions of laponite: New insights into the ageing phenomena,” *Proc. R. Soc. A*, vol. 464, no. 2090, pp. 469–489, 2007.

[65] H. Fam, J. T. Bryant, and M. Kontopoulou, “Rheological properties of synovial fluids,” *Biorheology*, vol. 44, no. 2, pp. 59–74, 2007.

[66] A. A. Madkhali, “Osteoarthritic synovial fluid rheology and correlation with protein concentration,” Master’s thesis, University of British Columbia, 2013.

[67] L. Mundt and K. Shanahan, “Graff’s Textbook of Urinalysis and Body Fluids,” 2nd ed., Lippincott Williams & Wilkins, 2010, pp. 253–262.

[68] “Arthritis Society,” 2018. [Online]. Available: https://www.arthritis.ca/. [Accessed: 22-Sep-2018].

[69] “Arthritis Foundation,” 2018. [Online]. Available: https://www.arthritis.org/. [Accessed: 22-Sep-2018].

[70] “Hospital for Special Surgery,” 2018. [Online]. Available: https://www.hss.edu/. [Accessed: 22-Sep-2018].

[71] V. L. Johnson and D. J. Hunter, “The epidemiology of osteoarthritis,” *Best Pract. Res. Clin. Rheumatol.*, vol. 28, no. 1, pp. 5–15, 2014.

[72] E. M. and W. D., “Efficacy of a natural mineral complex in north American adults with osteoarthritis of the knee: A randomized double-blind placebo-controlled study,” *Open Access Rheumatol. Res. Rev.*, vol. 6, pp. 91–103, 2014.

[73] P. Bhuanantanondh, D. Grecov, and E. Kwok, “Rheological study of viscosupplements and synovial fluid in patients with osteoarthritis,” *J. Med. Biol. Eng.*, vol. 32, no. 1, p. 12, 2012.

[74] P. Bhuanantanondh, D. Grecov, E. Kwok, and P. Guy, “Rheology of osteoarthritic synovial fluid mixed with viscosupplements: A pilot study,” *Biomed. Eng. Lett.*, vol. 1, no. 4, pp. 213–219, 2011.

[75] D. Mazzucco, G. H. McKinley, R. Scott, and M. Spector, “Rheology of Joint Fluid in Patients Undergoing Total Knee Arthroplasty,” *J. Orth. Res.*, vol. 20, pp. 1157–1163, 2002.

[76] D. Mazzucco, R. Scott, and M. Spector, “Composition of joint fluid in patients undergoing total knee replacement and revision arthroplasty: Correlation with flow properties,” *Biomaterials*, vol. 25, no. 18, pp. 4433–4445, 2004.

[77] M. Chernos, D. Grecov, E. Kwok, S. Bebe, O. Babsola, and T. Anastassiades, “Rheological study of hyaluronic acid derivatives,” *Biomed. Eng. Lett.*, vol. 7, no. 1, pp. 17–24, 2017.

[78] V. L. Johnson and D. J. Hunter, “The epidemiology of osteoarthritis,” *Best Pract. Res. Clin. Rheumatol.*, vol. 28, no. 1, pp. 5–15, 2014.

[79] L. Sharma, C. Lou, S. Cahue, and D. D. Dunlop, “The mechanism of the effect of obesity in knee osteoarthritis: the mediating role of malalignment,” *Arthritis Rheum*, vol. 43, no. 3, pp. 568–575, 2000.

[80] I. Reimann, J. Stougaard, and A. Northeved, “Measurement of the viscosity of synovial

fluid," *Scand. J. Rheumatol.*, vol. 4, no. 1, pp. 43–48, 1975.

[81] P. Bhuanantanondh *et al.*, "Rheology of Synovial Fluid With and Without Viscosupplements in Patients With Osteoarthritis : A Pilot Study," Master's thesis, University of British Columbia, 2009.

[82] K. M. . Oates, W. E. Krause, R. L. Jones, and R. H. Colby, "Rheopexy of synovial fluid and protein aggregation," *J. R. Soc. Interface*, vol. 3, no. 6, pp. 167–174, 2006.

Appendices

Appendix A : Capillary Flow of Generalized Newtonian Fluid with Slip at the Walls

General equation for the flow rate of a fully developed and incompressible flow in a circular tube, subject to slip at the wall location can be formulated as follows:

$$Q = \pi R^2 U_s(\tau_w) + 2\pi \int_0^R \dot{\gamma}(r) r dr \quad \text{(A1)}$$

where Q, R, U_s, τ_w, $\dot{\gamma}$ are the flow rate, radius of the tube, slip velocity, wall shear stress and shear rate respectively, and the fluid is flowing in the z direction. The first term in Equation A1 is associated with the flow rate due to slip, Q_s. In order to relate the shear rate with shear stress, the integration variable, r, can be replaced by τ_{rz} via $\tau_{rz} = \tau_w(r/R)$. Using integration by parts for the second term, Equation A1 would become:

$$\frac{4(Q-Q_s)}{\pi R^3} = \frac{4}{\tau_w^3} \int_0^{\tau_w} \dot{\gamma}(\tau_w) {\tau_{rz}}^2 d\tau_{rz} \quad \text{(A2)}$$

where $\dot{\gamma}(\tau_w)$ is the true shear rate at the wall. The left term is known as the apparent shear rate, $\dot{\gamma}_a$. The integral can be eliminated by taking the derivative of both sides with respect to τ_w and using the Leibniz rule of integration as follows:

$$\frac{\partial}{\partial \tau_w}(\dot{\gamma}_a \tau_w^3) = \frac{\partial}{\partial \tau_w} \int_0^{\tau_w} 4\dot{\gamma}(\tau_w) {\tau_{rz}}^2 d\tau_{rz} + 4\dot{\gamma}(\tau_w)\tau_w^2 \quad \text{(A3)}$$

Thus, the slip-corrected shear rate, $\dot{\gamma}(\tau_w)$, with regards to the wall shear stress, τ_w, can be formulated as:

$$\dot{\gamma}_w(\tau_w) = \dot{\gamma}_{true} = \frac{\dot{\gamma}_a}{4}\left[3 + \frac{d\ ln(\dot{\gamma}_a)}{d\ \ln(\tau_w)}\right] \tag{A4}$$

The corrected shear rate formulation is valid for any type of power-law generalized Newtonian fluid flow inside a straight circular tube [4], [11].